

Impacts of Very Small Initial Condition Errors on Mesoscale Aspects of Two Cyclones

MARTIN A. BAXTER

Central Michigan University, Dept. of Geology and Meteorology, Mt. Pleasant, Michigan

(manuscript received 20 September 2010, in final form 31 January 2011)

ABSTRACT

The atmosphere's sensitive dependence to initial conditions dictates that errors at the smallest resolvable scales of the model grow upscale to degrade the accuracy of larger scale motions. Even infinitesimal errors in the initial conditions can lead to errors in the prediction of mesoscale structures within one to two days lead time. Previous research demonstrates that upscale error growth is more rapid in the presence of moist convection, and that variability in this error growth exists among convective events. To investigate the role this variability in error growth might play in the forecast process, forecasts were conducted using the WRF-ARW for two cases of cyclogenesis featuring convection. Two 36 km forecasts for each case were created, a control run and a perturbation run in which the initial temperature field is perturbed. While both cases feature convection, the perturbations lead to larger error magnitudes and more significant upscale error growth in the February case. This is thought to be due to the tendency of the convection to be collocated with regions where gravity waves will propagate error energy upstream. Control and perturbation runs for the February event were conducted at 12 km resolution. These runs feature faster upscale error growth than the 36 km runs.

1. Introduction

Predictability is defined as “the extent to which future states of a system may be predicted based on knowledge of current and past states of a system” (Glickman 2000). Predictability can be conceptualized in two ways, in terms of “intrinsic predictability” and “practical predictability” (Zhang et al. 2006, after Lorenz 1996). Forecast errors associated with intrinsic predictability can be thought of as “unavoidable”, as these “intrinsic errors” arise due to the atmosphere's sensitive dependence to initial conditions. Forecast errors associated with practical predictability are “avoidable”, as the errors arise due to the quality of the observations and model. The latter errors may be rectified in the future through advances in scientific understanding.

Corresponding author address: Martin A. Baxter, Dept. of Geology and Meteorology, Central Michigan University, 314 Brooks Hall, Mt. Pleasant, MI 48859.
E-mail: baxtelma@cmich.edu

The range of predictability is defined as the time it takes initial condition errors at the smallest resolvable scales of the model to grow and contaminate the skill remaining in the larger scales (Lorenz 1969, Leith and Kraichnan 1972). Certain atmospheric situations may be more or less sensitive to the initial conditions, meaning that different scenarios are inherently more or less predictable. Model experiments illustrate that small-scale errors will grow most rapidly in regions of moist convection (Zhang et al. 2002, Zhang et al. 2003). Thus, situations involving moist convection are associated with a larger amount of intrinsic error and are inherently less predictable. The aforementioned works illustrate that as forecast lead time increases, errors propagate upscale, transitioning from unbalanced flow at convective scales to balanced flow at larger scales. Moist convection is associated with changes in the mass and momentum fields that are non-linear in character. Within the model, these changes are represented by the triggering of parameterizations. For example, even a very small amplitude perturbation can cause a large response if it results in activation of the convective parameterization scheme. As model resolution increases and convective parameterization is no longer used, non-linearities in other schemes will be responsible for error growth.

The rate of error growth is also related to the location of moist convection with respect to baroclinic zones. Zhang (2005) demonstrates that reduced predictability arises when an upper-level potential vorticity gradient becomes inseparable from a mid-level, diabatically-produced region of potential vorticity. Zhang et al. (2007) provide a three-stage description of error growth characteristics. First, errors quickly saturate the convective scales. Next, errors transform into balanced motions. This stage is referred to as “transitional”, as part of the errors are in the form of balanced motions, while others are radiating away from their source regions in the form of

gravity waves. In the final stage, errors within the balanced flow grow with the baroclinic instability of the background flow.

There exists variability in the extent to which errors will propagate upscale within events featuring convection. Hohenegger et al. (2006) analyzed three events, each featuring convection moving at varying speeds. Hohenegger et al. (2006) illustrate that merely investigating the characteristics of convective instability does not allow the degree of predictability to be inferred. The length of time that errors are actively growing will play a large role in determining the extent of upscale error propagation in an event. The mechanism for error propagation appears to be gravity waves. If the background flow is strong in comparison to the gravity wave speed, the errors will move away from the area of moist convection that is generating them, and they will not feed back on new convective development. If the background flow is weak in comparison to the gravity wave speed, errors will *not* move away from their region of generation, and will thus grow upscale.

The resolution of the model will also influence the rate at which errors grow in magnitude and scale. Ancell and Mass (2006) find that the low-level pressure field is sensitive to lower-tropospheric, upshear-tilted, subsynoptic scale, wave-like features in the temperature field. As model resolution increases, these features decrease in scale and spatial extent, and the error growth rates increase as well. While Ancell and Mass (2006) make use of an adjoint model to evaluate the resolution dependency, Zhang et al. (2002, 2003) arrive at similar conclusions by applying small-scale perturbations to the temperature field in simulations of varying resolutions.

This study will focus on three aspects of mesoscale predictability. First, the differences in upscale error growth for two events featuring moist convection moving at varying speeds will be

investigated. Next, the relationship between gravity waves and the background flow in determining the potential for sustained error growth will be evaluated. Finally, the effects of decreasing the model grid spacing on upscale error growth will be examined. Section two is an overview of the data and methods used. An analysis of the intrinsic predictability of two cases is presented in sections three and four, using model simulations at 36 km and 12 km, respectively. Section five discusses the results and concludes the work.

2. Data and Methodology

Two cases were selected that feature developing cyclones and warm-sector convection. The December 22-23, 2007 event features convection that moves rapidly across the model domain at approximately 70 km h^{-1} . The February 12-13, 2008 event features convection that moves more slowly across the model domain at approximately 45 km h^{-1} . Events were simulated using Version 2.2 of the Weather Research and Forecasting – Advanced Research model (hereafter WRF), developed at the National Center for Atmospheric Research (Skamarock et al. 2008). 48-hour simulations were performed, first using a single 36 km domain and then a 12 km domain, with both domains encompassing the same area ([Fig. 1](#)). 50 levels in the vertical were used, with a model top of 100 mb. The initial condition was from the 12 km North American Model (NAM; Janjić 2003), and the boundary conditions were from the 0.5° Global Forecast System (GFS; NCEP 2003) initialized 6 hours prior to the initial condition. Parameterizations employed include the Lin et al. microphysics scheme (Chen and Sun 2002), Kain-Fritsch convective parameterization (Kain 2004), Yonsei University planetary boundary layer scheme (Hong et al. 2006), and the Dudhia shortwave (Dudhia 1989) and rapid radiative transfer model

longwave radiation (Mlawer et al. 1997) schemes. The December case was initialized at 0000 UTC 22 December 2007 (from here on, dates and times will be noted in the form of DD/HH UTC, e.g., 22/00 UTC), and the February case was initialized at 0000 12 February 2008 (12/00 UTC).

For each event, two forecasts were created, a control run and a perturbation run. The experimental design follows the “perfect model” approach, where the initial conditions of the control run are modified to create a perturbation run. The evolution of the model runs were compared, with the differences due solely to the modification of the initial condition. These differences will henceforth be referred to as “errors”, as the control run is assumed to be perfect. The modification to the initial condition consists of the addition of random noise (a Gaussian distribution with a zero mean and standard deviation of 0.2 K) to the temperature field at all grid points in the model domain ([Fig. 2](#)). The same noise field was used in both 36 km experiments, and a new field is generated for the 12 km experiment, as more values were required for the larger number of grid points. The amplitude of the noise follows that of Tan et al. (2004), as used in a similar experiment involving an idealized baroclinic wave simulated at 30 km grid spacing.

The approach used to evaluate the duration of the error growth phase follows that of Hohenegger et al. (2006). The horizontal component of the group velocity of gravity waves in two-dimensional (x-z) flow of horizontal velocity U_0 is given by [see Holton (2004), his Eq. (7.45a)]:

$$c_{gx} = \pm \frac{Nm^2}{(m^2 + k^2)\sqrt{m^2 + k^2}} + U_0 \quad (1)$$

where N is the square root of the Brunt-Vaisala frequency and k and m denote horizontal and vertical wavenumbers, respectively. In arriving at the expression above, the flow is assumed to be dry, with uniform profiles of static stability and wind speed, no friction, and neglect of the Coriolis force. For upstream propagation of error energy to occur via gravity waves, c_{gx} must be of opposite sign of the component of the flow in the x-direction, U_0 , meaning that:

$$U_0 \leq \frac{Nm^2}{(m^2 + k^2)\sqrt{m^2 + k^2}} = U_{crit} \quad (2)$$

where U_{crit} represents the maximum wind velocity allowing upstream energy propagation via gravity waves. Note that the theoretical expression for the gravity waves is valid only for two-dimensional flow. Thus, the flow U_0 includes only the east-west component of the total flow. This limitation results in a more qualitative assessment, though the convection does move primarily from east to west in both cases. 10 km was selected for λ_z and 300 km was selected for λ_x . The use of deeper thermal perturbations resulted in similar outcomes. 300 km represents the approximate average wavelength of upper-level thermal temperature errors, with differing values resulting in similar conclusions. Values of U_0 and N were averaged over half of a vertical wavelength. While the formulation of c_{gx} is simplified, the approach has been shown to contribute to effective delineation of the variability in predictability amongst different events. The reader is directed to Holton (2004) and Hohenegger et al. (2006) for further information on the methodology employed here. For further information regarding the influence of static stability and baroclinicity on the characteristics of gravity waves, the reader is directed to Wang and Zhang (2007). The remainder of the text will use the term “gravity waves”, which refer to the assumed gravity waves as previously defined.

Error fields between the control and perturbation runs were analyzed. To summarize the evolution of errors over the full domain, an integrated metric was used, as first employed in Zhang et al. (2002). The difference total energy (DTE) per unit mass is defined by:

$$\frac{1}{2} \sum (U'^2_{ijk} + V'^2_{ijk} + \kappa T'^2_{ijk}) \quad (3)$$

where U' , V' , and T' are differences in the wind and temperature in the two runs, and $\kappa = C_p/T_r$ (where T_r is the reference temperature used in the model, 287 K). The summation occurs over all grid points in x , y , and σ . A spectral analysis was performed, providing the amount of total variability of the DTE accounted for by each wavelength in the space domain. Thus, this analysis allows the amount of upscale propagation of the initial error to be evaluated. Further details on the method used for this analysis can be found in Errico (1985).

3. 36 km Forecasts

a. December 2007 event

At 22/00 UTC, a surface low pressure system resides in western Texas ([Fig. 3](#)). Through the next 12 h, this surface low moves eastward, while new lows develop in Iowa and Minnesota. By 23/00 UTC, a line of convection has formed in advance of the southernmost surface low as it undergoes cyclogenesis. Over the next 24 h, the lows in the south and north merge over the western Great Lakes, and the line of convection moves to the eastern U.S away from the surface low. The evolution of model forecast MSLP and simulated reflectivity is shown in [Fig. 4](#). Differences in the MSLP and simulated reflectivity between the control ([Fig. 5a](#)) and

perturbation runs ([Fig. 5b](#)) are not meteorologically significant, although subtle variation in the simulated reflectivity is seen.

The accumulation of model simulated precipitation every 3 h ([Fig. 6a](#)) indicates precipitation in excess of 40 mm to the northwest of the surface low, with minimal precipitation along the convective line until it has moved over the eastern Great Lakes. The 4 km Stage-IV precipitation data (Lin and Mitchell 2005) highlights the considerable detail that is missing from the 36 km simulation ([Fig. 6b](#)). Errors in the accumulated precipitation ([Fig. 7](#)) first appear near northeastern Minnesota 9 h into the forecast at 22/09 UTC. By 22/21 UTC, errors are seen in eastern Kansas. These precipitation errors are associated with shifts in the location of precipitation features. Through the remainder of the forecast, errors spread to the northeast, appearing first in the vicinity of the surface cyclone in Wisconsin, and later near the convective line in the eastern Great Lakes.

The precipitation errors at 22/21 UTC in western Kansas occur to the northwest of an area of negative lifted index and convective precipitation ([Fig. 8](#)). The precipitation errors are located downstream from the base of the 300 mb trough, and are collocated with the initial appearance of errors in the 300 mb temperature. Through 23/12 UTC, 300 mb temperature errors continue to increase in magnitude in an area of ridging immediately downstream from the base of the trough in northern Wisconsin. It is apparent that the scale of the temperature errors fluctuates with time, as the distance between the minima and maxima varies with time. An area of negative lifted index (LI) is present in southern Wisconsin at 23/09 UTC, though the precipitation produced by the model does not come from the convective parameterization scheme. A concomitant decrease in scale of the temperature error is observed, indicating that

production of new errors may be occurring. Errors in temperature continue to be observed near the closed low through the end of the forecast period, and new errors are apparent north of the convective line as it moves eastward (at 23/21 UTC). In summary, the initial forecast errors become separate from those associated with the line of convection as the convection moves rapidly away from the base of the trough.

It is interesting that the initial forecast differences retain their amplitude despite the fact that they become disconnected from the area of convection, where errors are generated. As presented in Zhang et al. (2007), once errors propagate to larger scales, they will be less affected by dissipation and will then evolve with the background baroclinic wave. The area masked in white in [Fig. 9](#) indicates where the propagation of energy contained in gravity waves is against the u component of the flow. Growing 300 mb temperature errors (from 12/21 UTC onward) are confined exclusively to this masked area, where winds are weak westerlies or easterly. In this region, errors transported via gravity waves are continually superimposed on the errors from earlier time steps. The errors are not transported downstream because of the weak flow. New error production appears to take place at 23/09 UTC in southern Wisconsin when earlier errors have already grown to larger scales, a phenomenon also noted by Zhang et al. (2007).

b. February 2008 event

At 12/00 UTC, a surface low in the Texas panhandle is connected to an east-west oriented stationary front that extends to South Carolina ([Fig. 10](#)). Over the next 12 h, new surface lows develop along this front, and convection forms just to its north. By 13/00 UTC, surface cyclogenesis ensues in Ohio and the stationary front has turned to a cold front along the Gulf

coast. Convection exists out ahead of this cold front, and a new area of convection has developed throughout Florida. Through the remainder of the forecast, these areas of convection advance northward up the eastern seaboard. The low in Ohio lifts to the northeast and decays, while a new cyclone forms along the Gulf coast and moves northward with the convection. As in the December case, the evolution of model forecast MSLP and simulated reflectivity ([Fig. 11](#)) is representative enough to the observations for the purposes of this analysis. Variation in the area of maximum reflectivity near eastern Massachusetts and variation in the areal extent of the 984 mb contour exist between the control ([Fig. 12a](#)) and perturbed simulations ([Fig. 12b](#)). These differences are more significant than those seen in the December simulations, though the magnitude of the differences does remain quite small in an absolute sense.

Maximum accumulated precipitation totals from the model ([Fig. 13a](#)) are twice as high in the February case versus the December case. The heaviest precipitation results when the convection from Florida moves up the eastern seaboard and merges with the convection that originated in Arkansas. The model simulates the axis of precipitation stretching from Texas northeast through Ohio more accurately than the precipitation stretching along the eastern seaboard ([Fig. 13b](#)). Precipitation errors ([Fig. 14](#)) appear earlier in the forecast than in the December case, 3 to 6 h into the forecast in western Texas. By 13/00 UTC, errors develop within the Gulf of Mexico and advance northward over the next 12 h. The dipole structure of the errors is indicative of a shift in the very narrow axis of precipitation along the east coast. It is apparent that this precipitation feature is highly unpredictable in terms of its exact location.

Slight errors in 300-mb temperature ([Fig. 15](#)) are seen in Texas 3 h into the forecast, in an area of negative LI and convective precipitation. Through 12/21 UTC, these errors continue to

develop in the area of advancing convective precipitation *without much increase in magnitude*, and appear to move further downstream from the base of the trough. At 13/00 UTC, errors increase in magnitude along the Gulf coast as the convection that began in Arkansas approaches the convection developing offshore. Through 13/06 UTC, errors again cease to grow in magnitude. At 13/09 UTC, increases in error magnitude are observed in Georgia and the Carolinas. Through the rest of the forecast, errors are maintained downstream from the base of the trough as the convection advances northward. Like the December case, the errors have not only increased in magnitude, but in scale as well. In summary, the errors remained coherent and focused in the area downstream from the trough. This is in contrast to the characteristics of the error evolution in the December case.

Despite the fact that convection is present throughout Oklahoma, Arkansas, and Texas from 12/03 through 12/21 UTC, 300 mb temperature errors do not grow in magnitude. This is likely due to the fact that the convection that is generating the errors is occurring where gravity waves will propagate the error energy downstream ([Fig. 16](#)). It is interesting to note that over this time period convection is relatively stationary, suggesting that the speed of propagating convection does not have a direct relationship to the duration of the error growth phase. It isn't until 12/21 UTC when the convection becomes collocated with an area of upstream energy propagation, and thus the error magnitude increases at 13/00 UTC. At 13/03 UTC, convection is confined primarily to the Gulf of Mexico away from any areas of upstream energy propagation, but by 13/06 UTC, convection and an area of upstream energy propagation advance into South Carolina and Georgia, resulting in renewed error growth that continues through 13/12 UTC. Following this, convection remains to the south of the area of upstream energy propagation, and

the temperature error magnitudes remain the roughly the same. As in the December case, when the area where gravity waves propagate against the flow is collocated with convection, error magnitudes will increase more rapidly.

c. DTE and Analysis of its Spectra

The evolution of DTE ([Fig. 17](#)) depicts a higher magnitude of errors in the February case throughout the forecast period. This result is consistent with the evolution of the 300 hPa errors discussed in section 3b. DTE peaks in the February forecast near FH39 (forecast hour 39; 13/15 UTC) and then begins to decrease, while the errors in the December case grow more gradually throughout the simulation. Closer examination of [Fig. 15](#) shows that after 13/15 UTC, errors in 300-mb temperature begin to move out of the domain, a possible explanation for the decline.

The peak of the curve of the DTE spectrum reveals the wavelength at which errors are most prominent. For the December case, errors are most prominent near 200 km at forecast hour (FH) 6, to near 400 km at FH 18 ([Fig. 18](#)). Beyond FH18, the error magnitude increases at a fairly constant rate, but the errors cease to grow upscale. As the lateral boundary conditions were not perturbed, there exists some constraint on the upscale growth of initial condition error, as discussed in Nutter et al. (2004). For the February case ([Fig. 19](#)), the errors are most prominent near 200 km at FH 6, and continue to propagate upscale to just greater than 1000 km at FH 42 and 48. Beyond FH 36, the magnitude of the errors generally decreases at all wavelengths.

4. 12 km Forecast

In the interest of brevity, only the 12-km results from the February 2008 case is presented here, as it featured the greater upscale error growth. The 12-km forecast amounts to a downscaled version of the 36 km forecast, as little differences in the MSLP and simulated reflectivity are apparent (compare [Fig. 20](#) with [Fig. 11](#)). Variation in the area of maximum reflectivity near Long Island, New York and variation in the magnitude of the lowest closed contour of MSLP (984 mb vs. 988 mb) exist between the control ([Fig. 21a](#)) and perturbed simulations ([Fig. 21b](#)). These are more significant differences than those seen in the 36 km simulation. Examination of the accumulated precipitation ([Fig. 22a](#)) from the model does reveal some differences in precipitation in the Gulf of Mexico and the eastern seaboard, in comparison with the 36 km forecast ([Fig. 13a](#)). Comparison with the observed precipitation ([Fig. 22b](#)) indicates that the 12 km forecast is more accurate than the 36 km domain with respect to the precipitation along the eastern seaboard. Precipitation errors ([Fig. 23](#)) evolve in the same manner as they did at 36 km, but they extend over a greater distance (compare with [Fig. 14](#)). The errors between the 12 km control and perturbation precipitation primarily represent shifts in the location of features. For example, the large precipitation errors off the New Jersey coast represent a difference in placement of 100 km. The evolution of the 300 mb temperature error ([Fig. 24](#)) is similar to that seen in the 36 km forecast, but is of higher magnitude, and appears to be on a larger scale, despite the decrease in model grid spacing. An evaluation of the gravity wave propagation is not presented here, as the fields used in the analysis exhibit no significant differences from those in the 36 km simulation.

The 12 km DTE field was interpolated to the 36 km grid for comparison ([Fig. 25](#)). Compared to the 36 km forecast, error growth in the 12 km forecast occurs at a faster rate, and

thus maintains a larger magnitude throughout the forecast. Unlike the 36 km simulation, the DTE continues to grow through the remainder of the forecast. It appears that less of the high magnitude errors are moving out of the domain in the 12 km forecast (see [Fig. 24](#)). The upscale error growth ([Fig. 26](#)) begins at near 100 km at FH 6, as the smallest scales that can be resolved by the 12 km grid are of shorter wavelength than those on the 36 km grid. By FH 36, the scale of the errors has reached nearly 1200 km in the 12 km forecast, but only about 600 km in the 36 km forecast. This is evidence of the errors propagating upscale more quickly in the higher resolution simulation. While the errors continue to propagate upscale in the 36 km simulation beyond FH 36, in the 12 km forecast the errors have essentially ceased to grow upscale by this point.

5. Discussion and Conclusions

This work employs the methods of predictability analysis first presented by Hohenegger et al. (2006) and Zhang et al. (2002, 2003), and finds them to be complementary in two “real” (non-idealized) events. The fact that the gravity wave analysis near regions of convection results in similar qualitative conclusions as the quantitative domain-averaged spectral analysis of DTE further strengthens the utility of this approach. In the cases analyzed here, convection moves through the domain, rather than being stationary, as was the case in the events analyzed by Hohenegger et al. (2006). Also, Hohenegger et al. (2006) present the gravity wave analysis for only one time period. The work presented here illustrates that increases (decreases) in error magnitude can be associated with the juxtaposition (or lack thereof) of the convection with the region where gravity waves will propagate upstream.

In both cases, error growth is observed between the 300 mb trough and ridge axis, similar to what is observed in the idealized simulations of Tan et al. (2004). In the December case, errors cease to propagate upscale after only 18 h. In the February case, errors continue to propagate upscale for 42 h. This contrast is likely related to the relationship between the location of the convection and the region where gravity waves will propagate upstream. In the December case, the convection was embedded in faster flow, thus the source of error generation *was never collocated* with an area where gravity wave energy would propagate upstream. In the February case, two separate episodes of convection were embedded in weaker flow, thus the source of error generation *was collocated* with an area where gravity wave energy would propagate upstream. It was also observed that merely evaluating the speed of the convection does not adequately determine the length of the error growth phase, as the February case featured several hours of stationary convection in which errors moved downstream via gravity waves. Although the cases presented here help support the hypothesis of Hohenegger et al. (2006), other possible hypotheses were not evaluated.

The comparison of upscale error growth for the 36 km and 12 km forecasts is in agreement with studies on the predictability of different scales of motion in the atmosphere (e.g., Ansell and Mass 2006, Zhang et al. 2002, 2003), which confirm earlier theoretical studies (e.g., Lorenz 1969, Leith and Kraichnan 1972). As models are designed to resolve smaller scale motions, the range of predictability is reduced. However, as model resolution increases, important physical processes are better resolved, resulting in improved forecasts. It remains to be seen how much forecast lead time is diminished due to the reduction in predictability necessitated by increasing resolution. The tendency for this to occur has been noted for the

ECMWF (Simmons and Hollingsworth 2002). Both cases illustrate that the locations of mesoscale precipitation features are very sensitive to the initial conditions, suggesting the potential utility of ensemble prediction systems designed for the mesoscale.

As observed in the cases presented here, the variability of intrinsic predictability is a function of model resolution and atmospheric scenario. Further understanding of these issues will lead to greater appreciation of the reasons for the variability in ensemble spreads, as well as better practices for the use of models of different resolutions.

Acknowledgements. The author thanks Fuqing Zhang (Penn State U.) for providing example Fourier Analysis code, and Charles Graves (Saint Louis U.) for assistance in modifying the code. Thank you to everyone who has participated in discussions during several lectures on Mesoscale Predictability I've given at the Cooperative Program for Operational Meteorology, Education, and Training, particularly James Hansen (Naval Research Laboratory), Ken Cook (NWS-Wichita, KS), and Josh Korotky (NWS-Pittsburgh, PA). Thank you to Rich Grumm (NWS-State College, PA) and one anonymous person for their thoughtful reviews. All images were generated with GEMPAK, Unidata's Integrated Data Viewer (IDV), and the Interactive Data Language (IDL) from ITTVIS.

REFERENCES

- Ancell, B. C. and C. F. Mass, 2006: Structure, growth rates, and tangent linear accuracy of adjoint sensitivities with respect to horizontal and vertical resolution. *Mon. Wea. Rev.*, **134**, 2971–2988.
- Chen, S.-H., and W.-Y. Sun, 2002: A one-dimensional time dependent cloud model. *J. Meteor. Soc. Japan*, **80**, 99–118.
- Dudhia, J., 1989: Numerical study of convection observed during the winter monsoon experiment using a two-dimensional mesoscale model. *J. Atmos. Sci.*, **46**, 3077–3107.
- Errico, R. M., 1985: Spectra computed from a limited area grid. *Mon. Wea. Rev.*, **113**, 1554–1562.
- Glickman, T. S., Ed., 2000: *Glossary of Meteorology*. 2nd Ed. American Meteorological Society, 855 pp.
- Hohenegger, C., D. Luthi, and C. Schar, 2006: Predictability mysteries in cloud-resolving models. *Mon. Wea. Rev.*, **134**, 2095–2107.
- Holton, J. R., 2004: *An Introduction to Dynamic Meteorology*. 4th ed. Academic Press, 535 pp.
- Hong, S.-Y., and Y. Noh, and J. Dudhia, 2006: A new vertical diffusion package with an explicit treatment of entrainment processes. *Mon. Wea. Rev.*, **134**, 2318–2341.
- Janjić, Z. I., 2003: A nonhydrostatic model based on a new approach. *Meteor. Atmos. Phys.*, **82**, 271–285.
- Kain, J. S., 2004: The Kain-Fritsch convective parameterization: An update. *J. Appl. Meteor.*, **43**, 170–181.
- Leith, C. E. and R. H. Kraichnan, 1972: Predictability of turbulent flows. *J. Atmos. Sci.*, **29**, 1041–1058.
- Lin, Y. and K. E. Mitchell, 2005: The NCEP Stage II/IV hourly precipitation analyses: Development and applications. Preprints, *19th Conf. on Hydrology*, Amer. Met. Soc., San Diego, CA.
- Lorenz, E. N., 1969: The predictability of a flow which possesses many scales of motion, *Tellus*, **21**, 289–307.

- Lorenz, E. N., 1996: Predictability- A problem partly solved. *Proc. Seminar on Predictability*, Vol. I, Reading, United Kingdom, ECMWF, 1-19.
- Mlawer, E. J., S. J. Taubman, P. D. Brown, M. J. Iaxono, and S. A. Clough, 1997: Radiative transfer for inhomogeneous atmosphere: RRTM, a validated correlated-k model for the long-wave. *J. Geophys. Res.*, **102 (D14)**, 16663-16682.
- NCEP, 2003: NCEP Office Note 442, The GFS atmospheric model, November, 2003, National Center for Environmental Prediction, Global Climate and Weather Modeling Branch, EMC, Camp Springs, Maryland
- Nutter, P., D. Stensrud, and M. Xue, 2004: Effects of coarsely resolved and temporally interpolated lateral boundary conditions on the dispersion of limited-area ensemble forecasts. *Mon. Wea. Rev.*, **132**, 2358–2377.
- Simmons, A.J. and A. Hollingsworth, 2002: Some aspects of the improvement in skill of numerical weather prediction. *Quart. J. Roy. Meteor. Soc.*, **128**, 647-677.
- Tan, Z.-M., F. Zhang, R. Rotunno, and C. Snyder, 2004: Mesoscale predictability of moist baroclinic waves: Experiments with parameterized convection. *J. Atmos. Sci.*, **61**, 1794–1804.
- Zhang, F., 2005: Dynamics and structure of mesoscale error covariance of a winter cyclone estimated through short-range ensemble forecasts. *Mon. Wea. Rev.*, **133**, 2876–2893.
- Zhang, F., C. Snyder, and R. Rotunno, 2002: Mesoscale predictability of the “surprise” snowstorm of 24-25 January 2000. *Mon. Wea. Rev.*, **130**, 1617-1632.
- Zhang, F., C. Snyder, and R. Rotunno, 2003: Effects of moist convection on mesoscale predictability. *J. Atmos. Sci.*, **60**, 1173-1185.
- Zhang, F., A. M. Odins, and J. W. Nielsen-Gammon, 2006: Mesoscale predictability of an extreme warm-season precipitation event. *Wea. Forecasting*, **21**, 146-166.
- Zhang, F., N. Bei, R. Rotunno, C. Snyder, and C. C. Epifanio, 2007: Mesoscale predictability of moist baroclinic waves: Convection-permitting experiments and multistage error growth dynamics. *J. Atmos. Sci.*, **64**, 3579-3594.

TABLES AND FIGURES

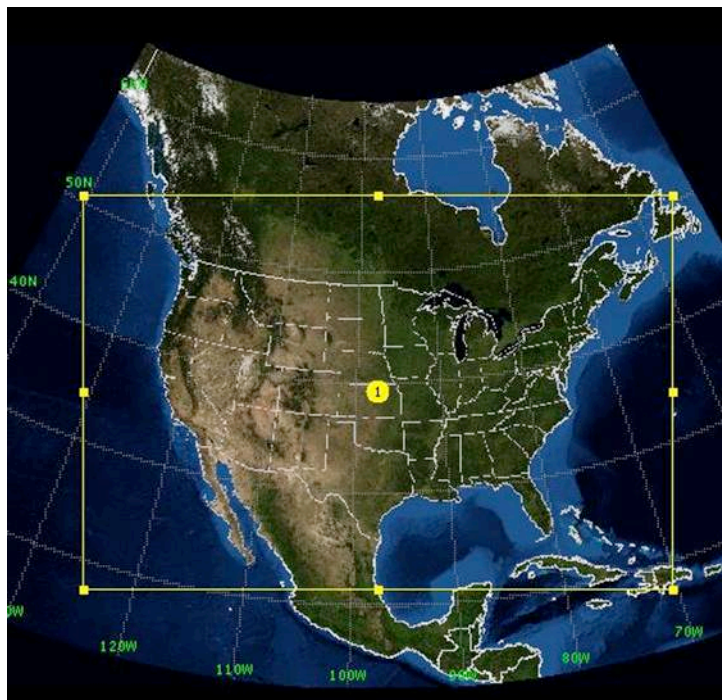


Figure 1. Model domain used for both the 36-km and 12-km forecasts.

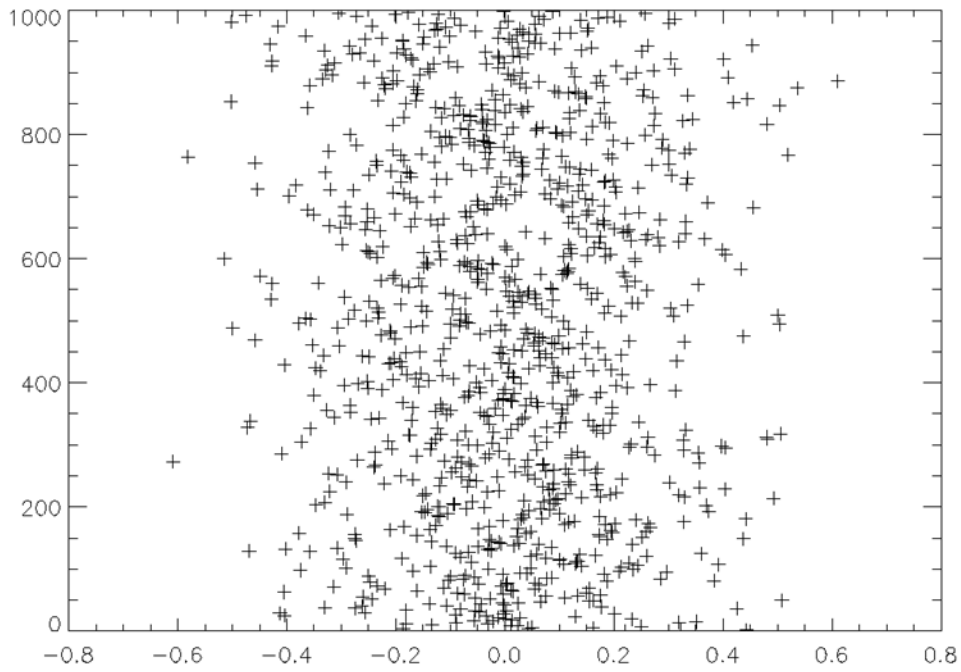


Figure 2. A sample of 1000 points from the distribution generated to define the perturbation.

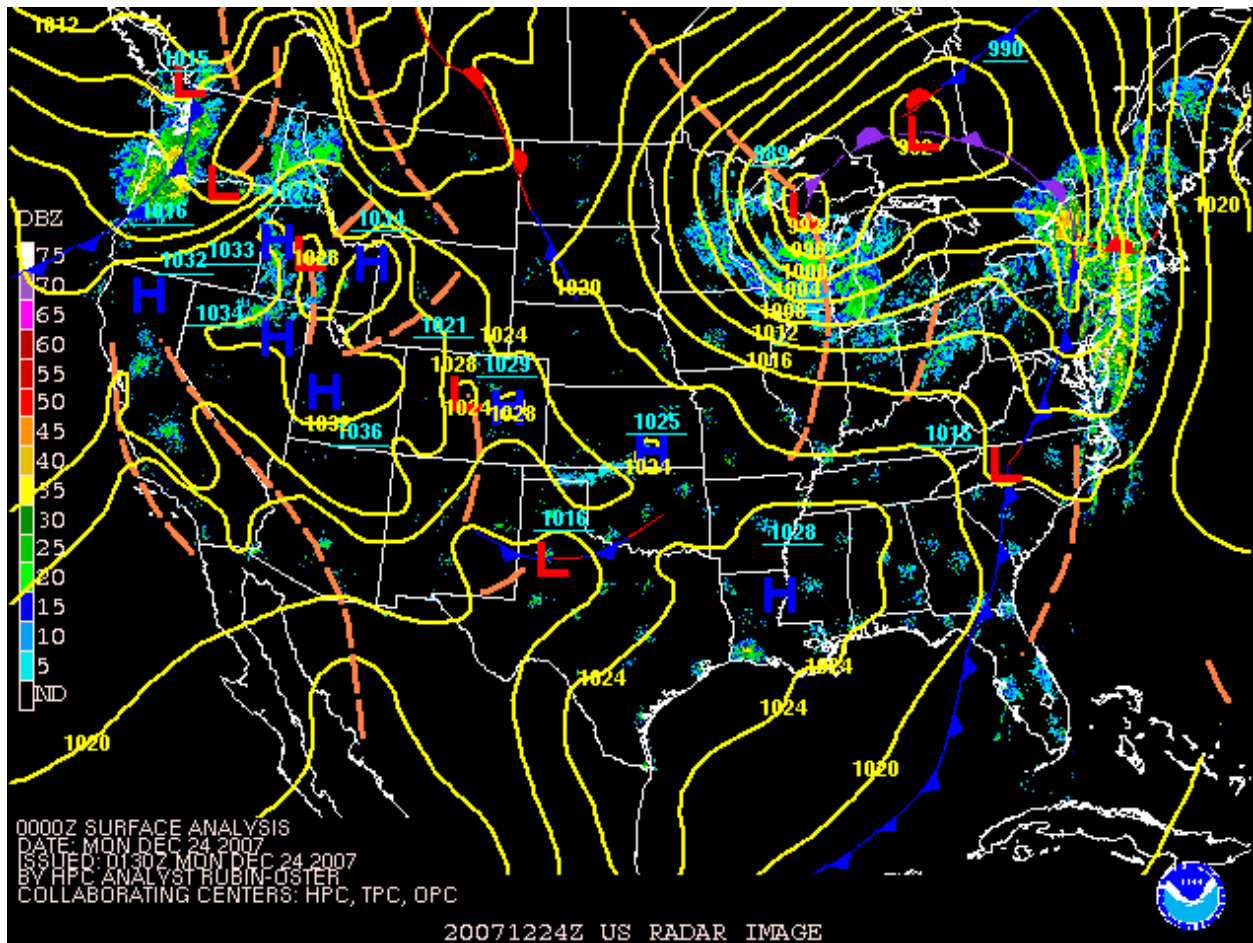


Figure 3. NCEP/HPC surface analysis overlaid on radar imagery (shaded; dBZ) spanning 0000 UTC 22 December 2007 through 0000 UTC 24 December 2007, animated in 3-h increments.

NOTE: This figure is an animation. A representative image is shown above. [Link to animation.](#)

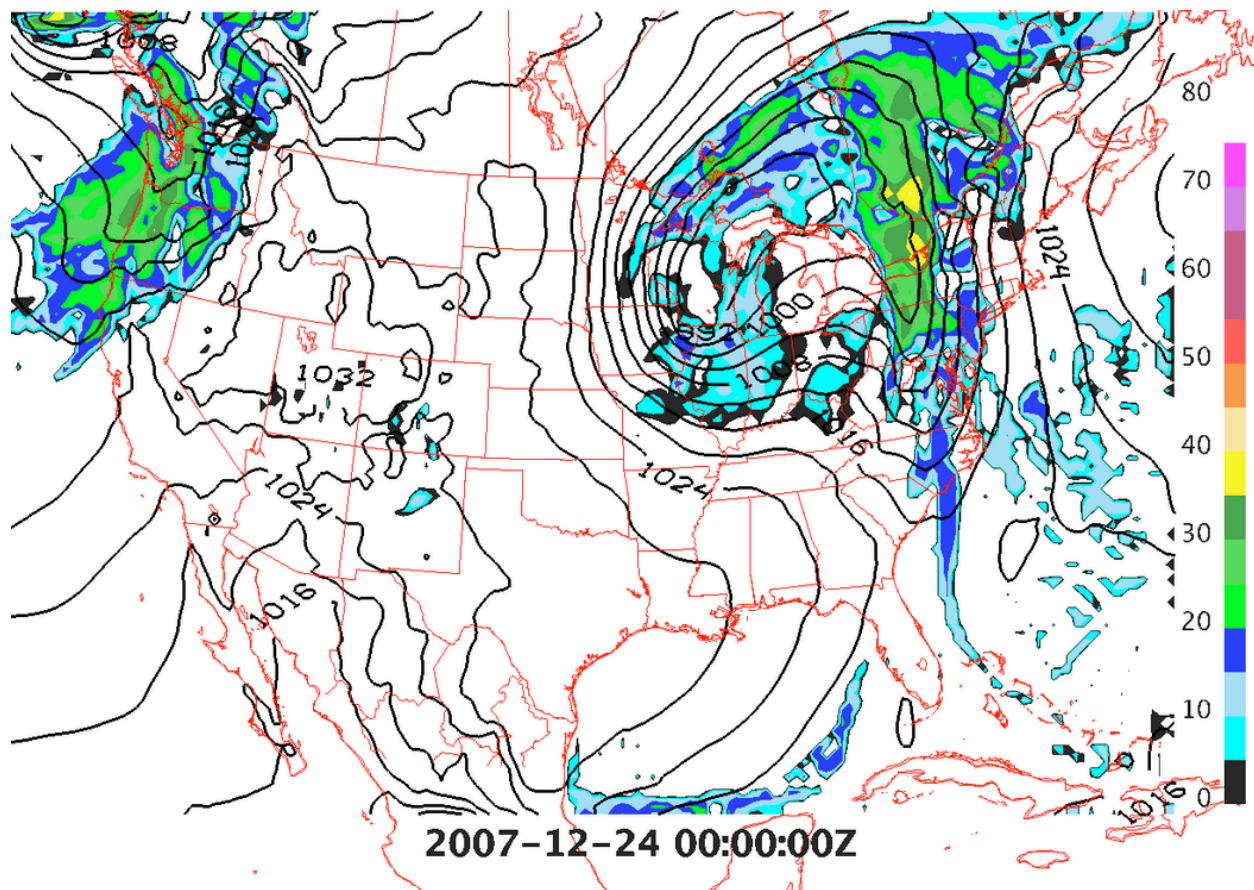


Figure 4. Model simulated mean sea level pressure (contours; 4 mb) and simulated reflectivity at 1 km (shaded; dBZ) spanning 0000 UTC 22 December 2007 through 0000 UTC 24 December 2007, animated in 3-h increments.

NOTE: This figure is an animation. A representative image is shown above. [Link to animation.](#)

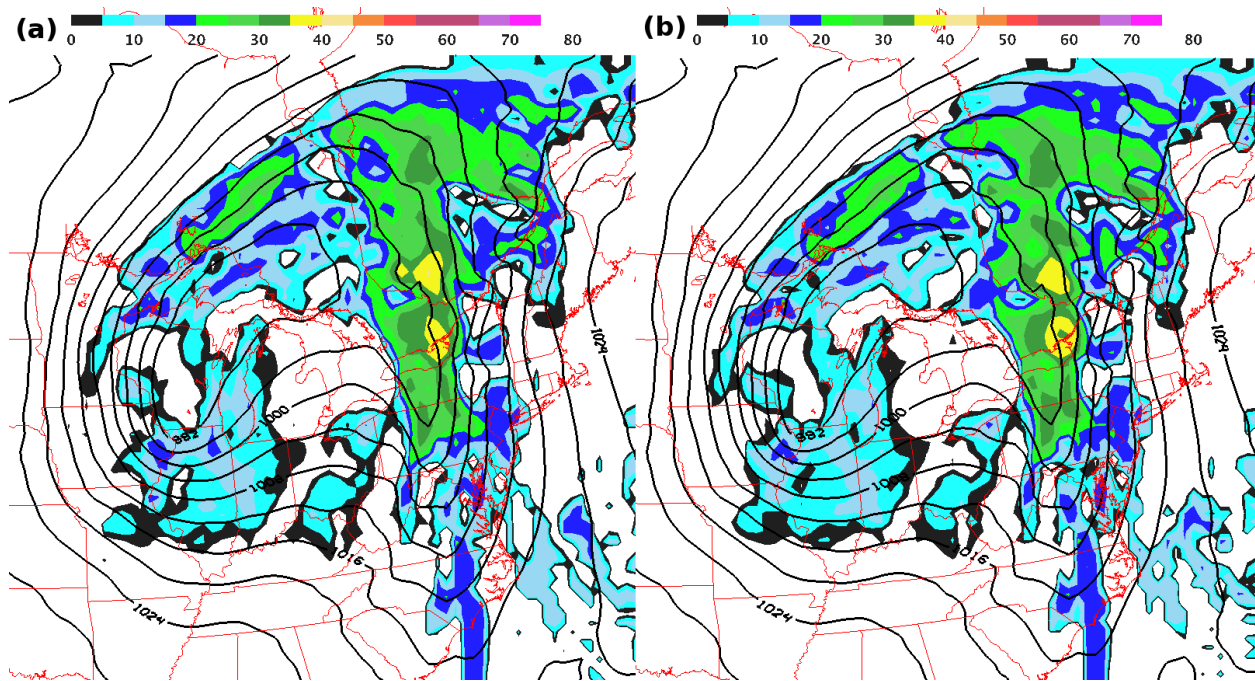


Figure 5. Model simulated mean sea level pressure (contours; 4 mb) and simulated reflectivity at 1 km (shaded; dBZ) for a 48-h forecast, valid at 0000 UTC 24 December 2007, for (a) control and (b) perturbation.

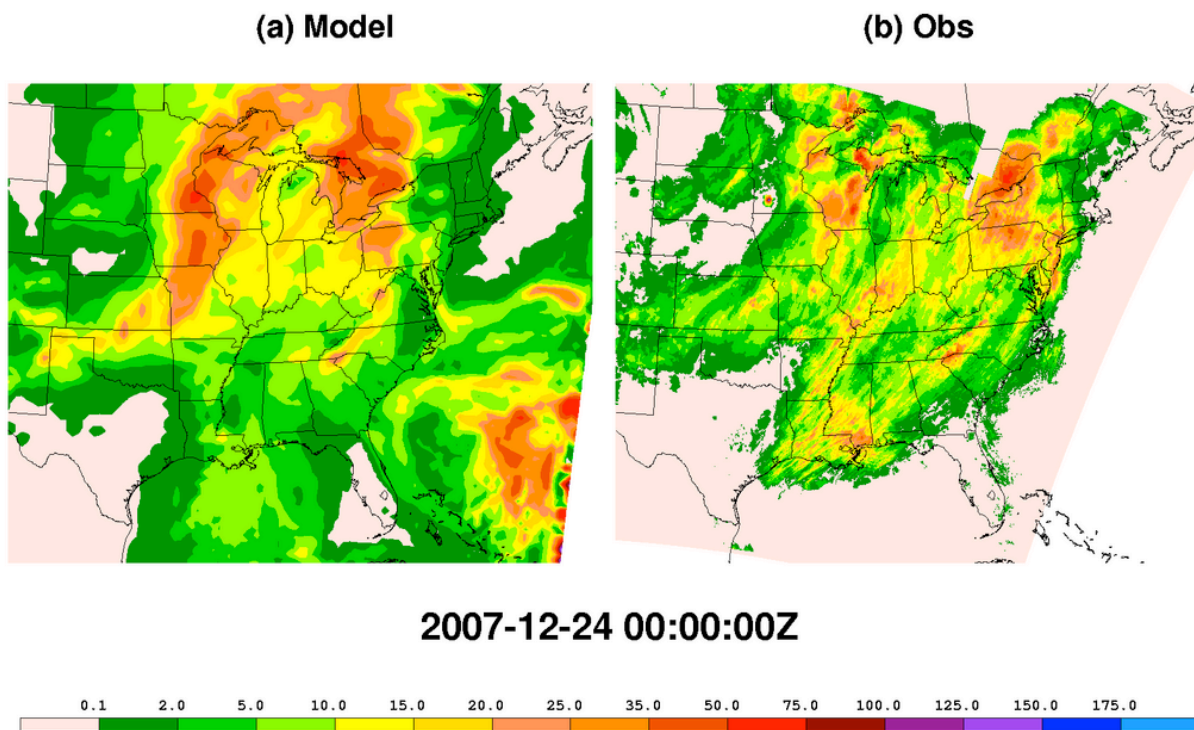


Figure 6. (a) Model accumulated precipitation (shaded; mm) and (b) Stage-IV QPE (shaded; mm) spanning 0000 UTC 22 December 2007 through 0000 UTC 24 December 2007, animated in 3-h increments.

NOTE: This figure is an animation. A representative image is shown above. [Link to animation.](#)

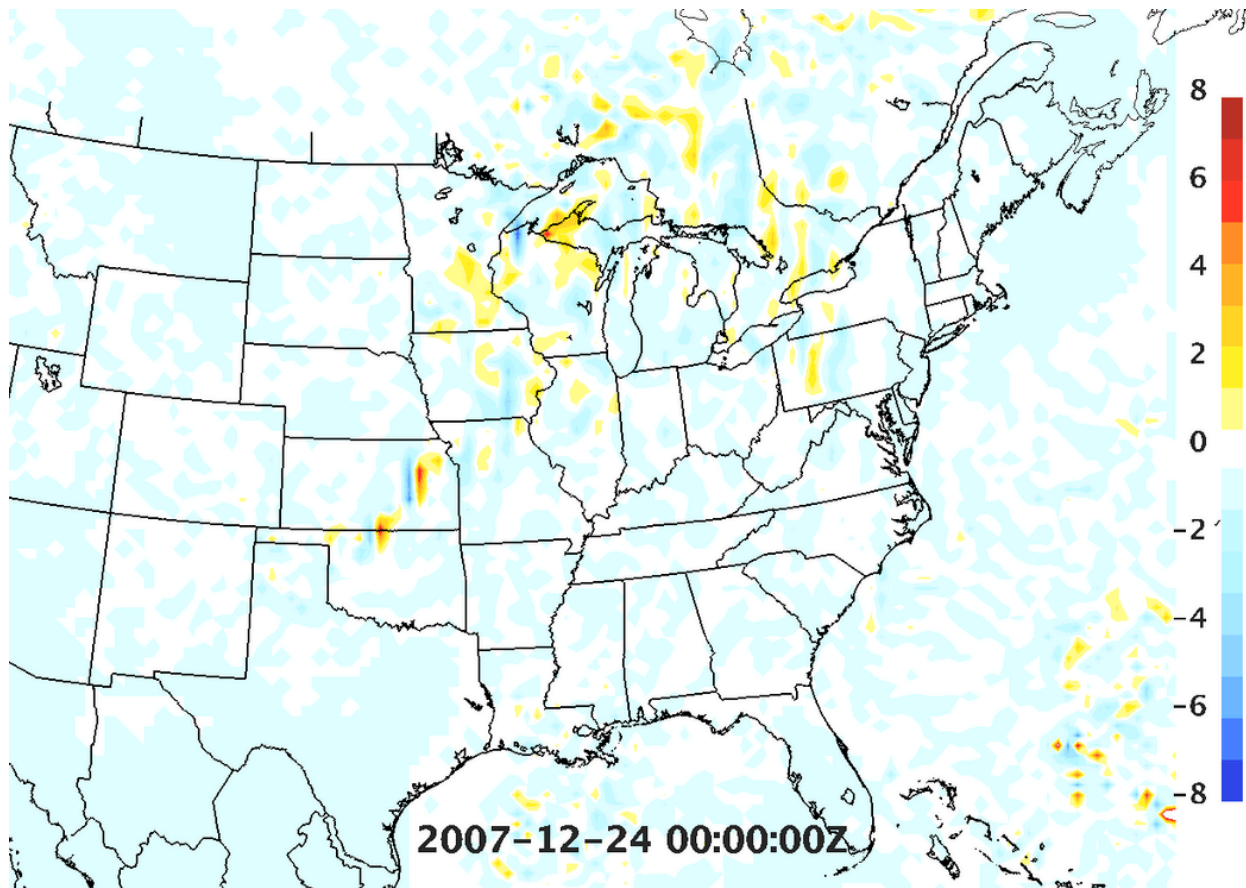


Figure 7. Accumulated precipitation error between control and perturbation runs (shaded; mm) spanning 0000 UTC 22 December 2007 through 0000 UTC 24 December 2007, animated in 3-h increments.

NOTE: This figure is an animation. A representative image is shown above. [Link to animation.](#)

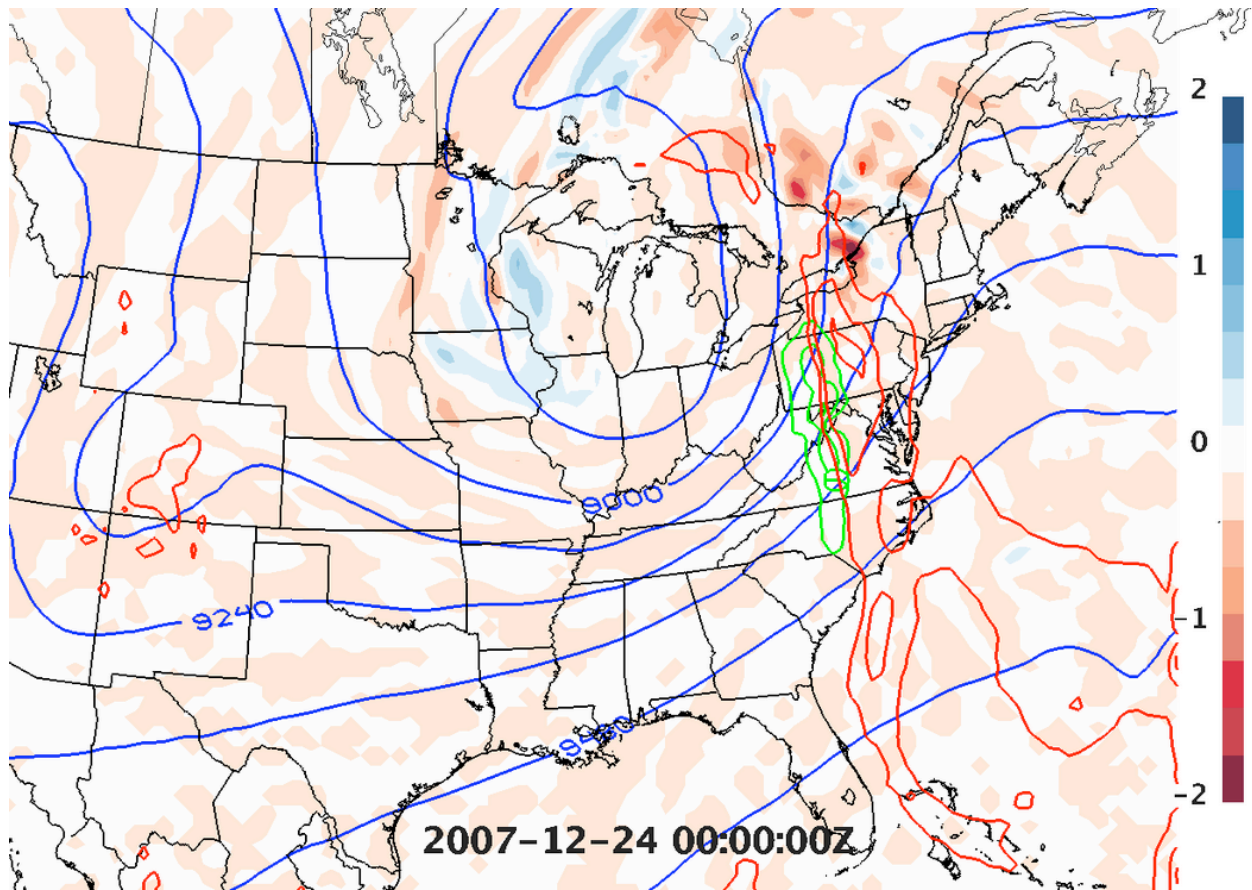


Figure 8. Heights at 300 mb (blue contours; 120 m), convective precipitation accumulated over 3 h (green contours; 3 mm, with 3 mm as first contour), lifted index (red contours; 2 K, only values of 2 K and below shown), 300 mb temperature error (control-perturbation; shaded; °C) spanning 0000 UTC 22 December 2007 through 0000 UTC 24 December 2007, animated in 3-h increments.

NOTE: This figure is an animation. A representative image is shown above. [Link to animation.](#)

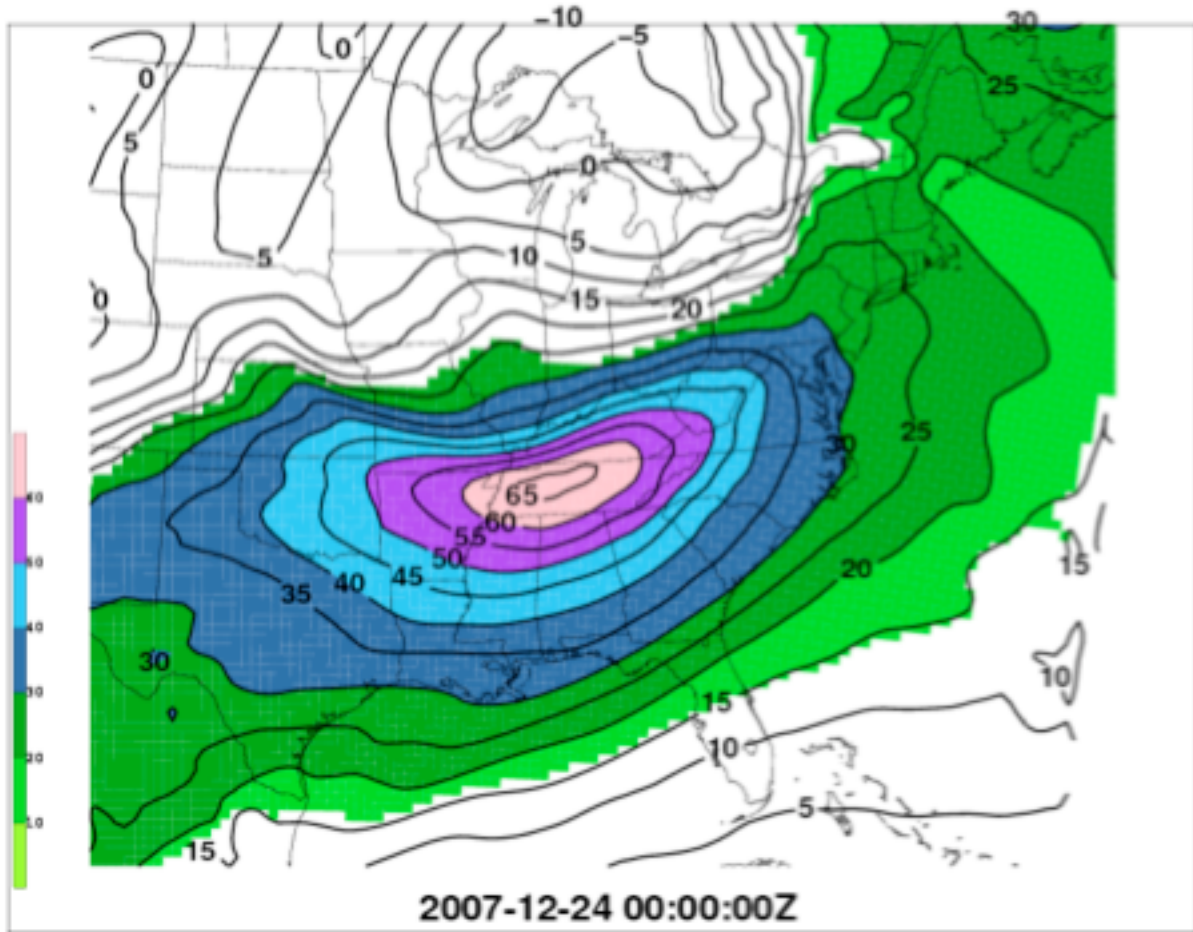


Figure 9. U-component of the wind, U_0 (shaded; m s^{-1}) averaged from 5 to 10 km, spanning 0000 UTC 22 December 2007 through 0000 UTC 24 December 2007, animated in 3-h increments. Values where U_0 are less than or equal to U_{crit} (indicating upstream error energy propagation) are masked in white.

NOTE: This figure is an animation. A representative image is shown above. [Link to animation.](#)

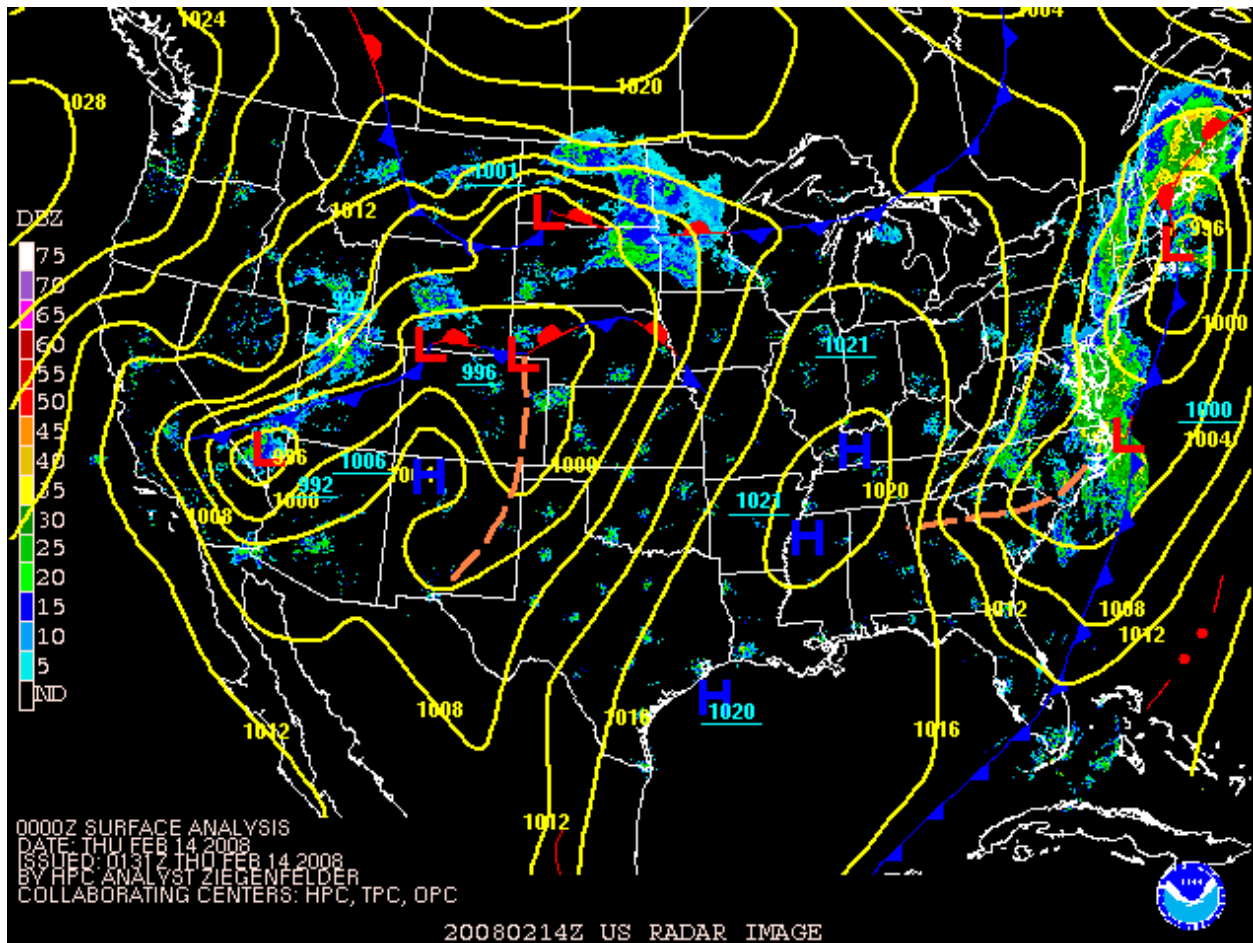


Figure 10. As in Fig. 3, but for 0000 UTC 12 February 2008 through 0000 UTC 14 February 2008, animated in 3-h increments.

NOTE: This figure is an animation. A representative image is shown above. [Link to animation.](#)

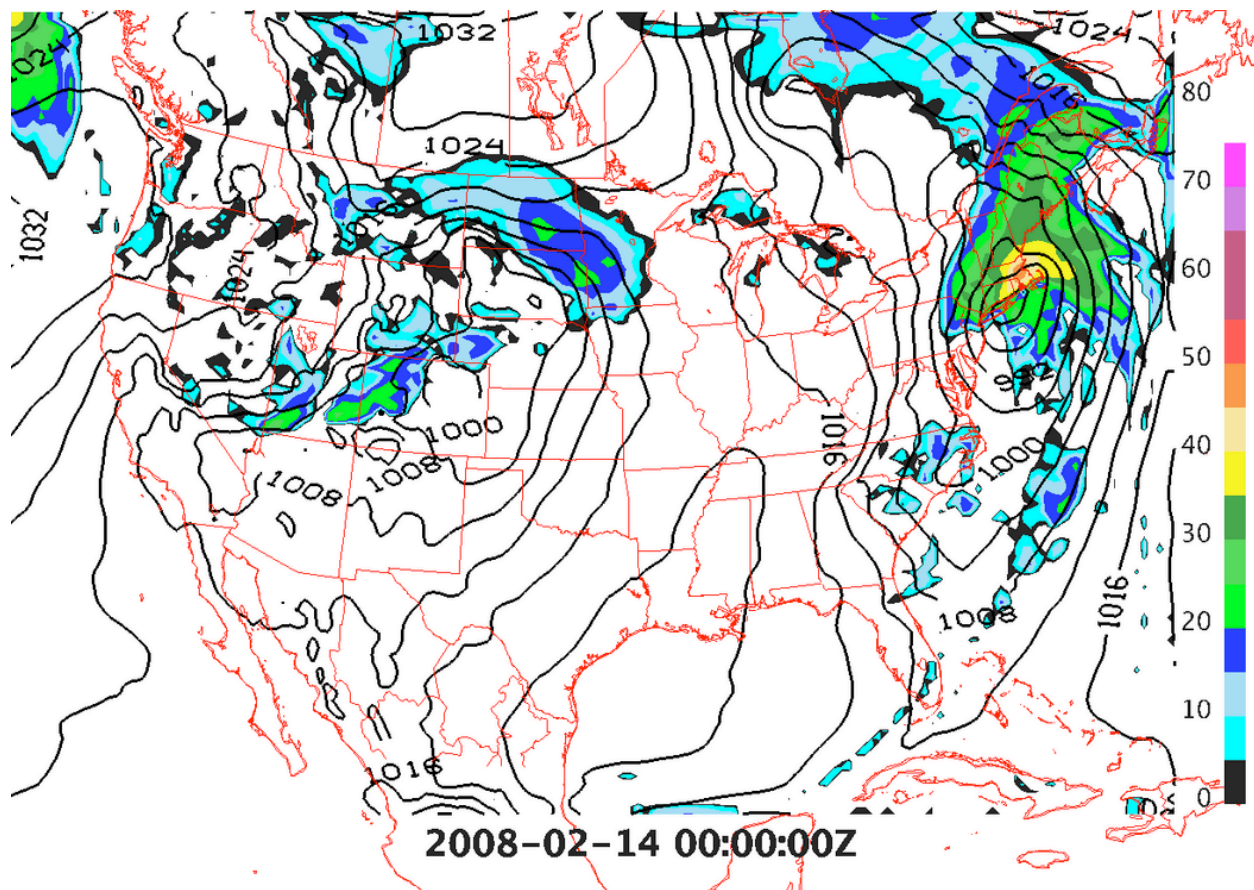


Figure 11. As in Fig. 4, but for 0000 UTC 12 February 2008 through 0000 UTC 14 February 2008, animated in 3-h increments.

NOTE: This figure is an animation. A representative image is shown above. [Link to animation.](#)

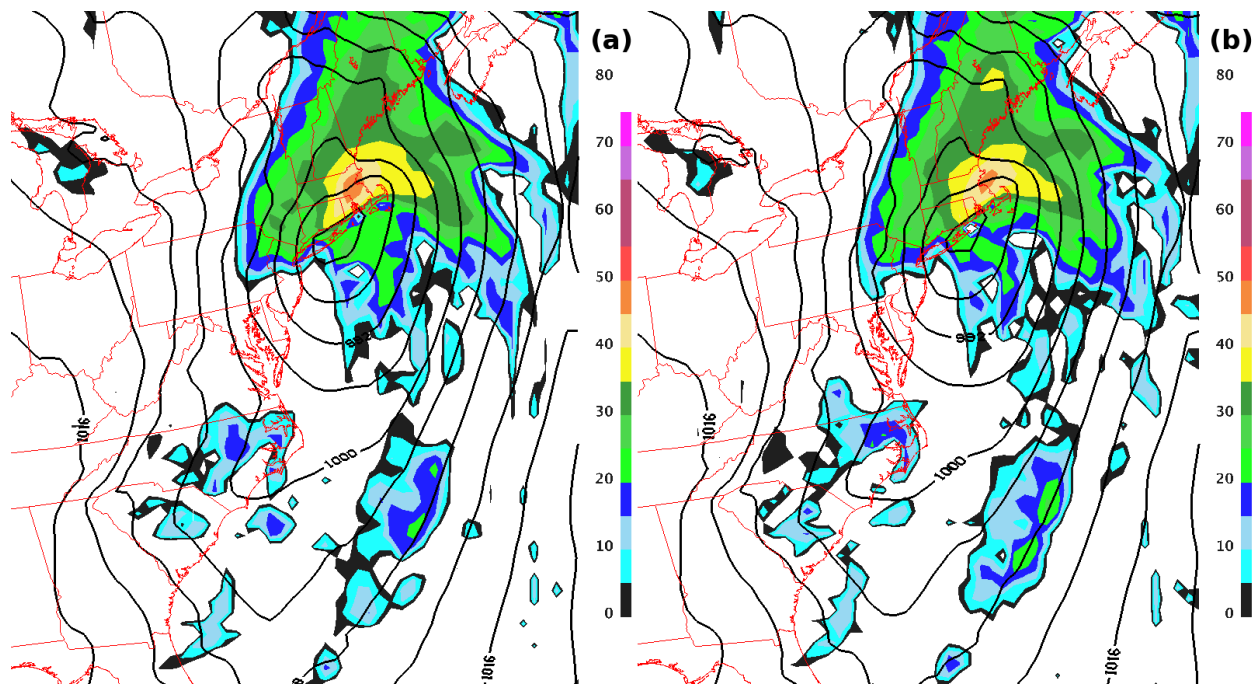


Figure 12. As in Fig. 5, but for a 48-h forecast, valid at 0000 14 February 2008.

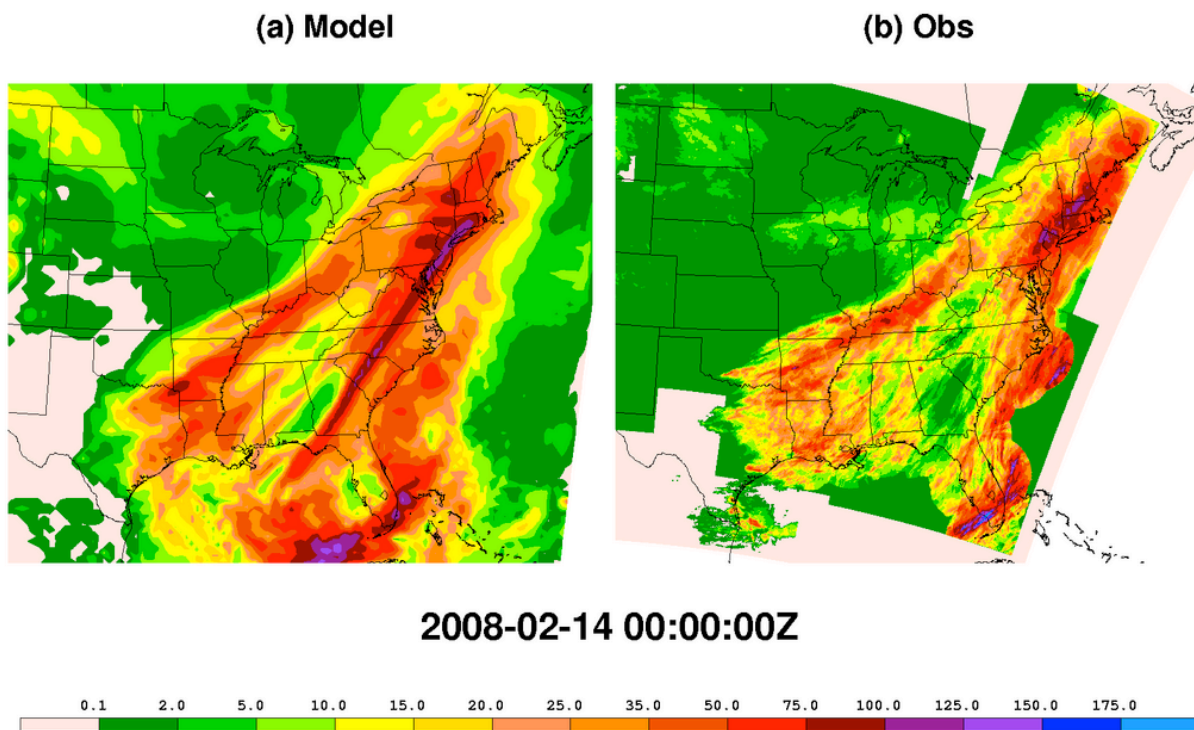


Figure 13. As in Fig. 6, but for 0000 UTC 12 February 2008 through 0000 UTC 14 February 2008, animated in 3-h increments.

NOTE: This figure is an animation. A representative image is shown above. [Link to animation.](#)

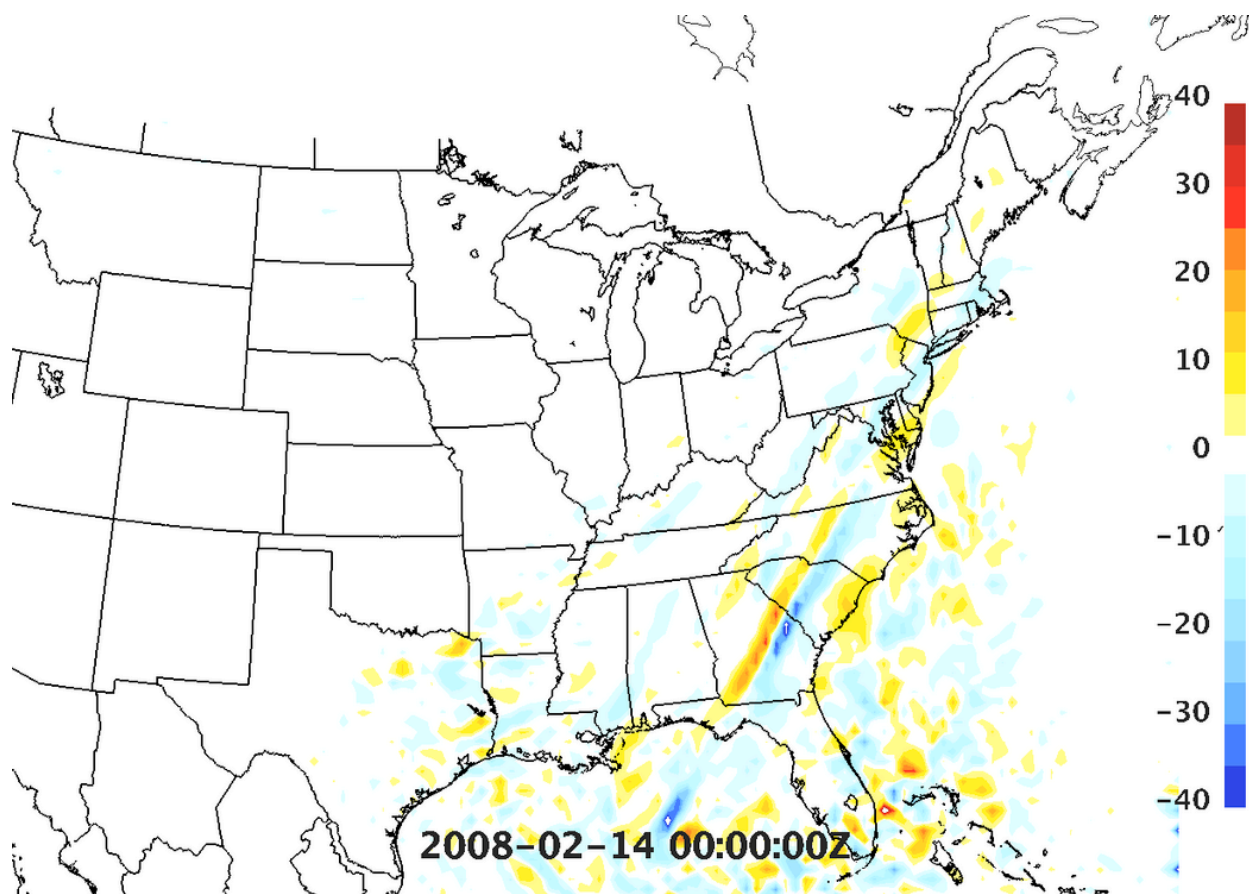


Figure 14. As in Fig. 7, but for 0000 UTC 12 February 2008 through 0000 UTC 14 February 2008, animated in 3-h increments.

NOTE: This figure is an animation. A representative image is shown above. [Link to animation.](#)

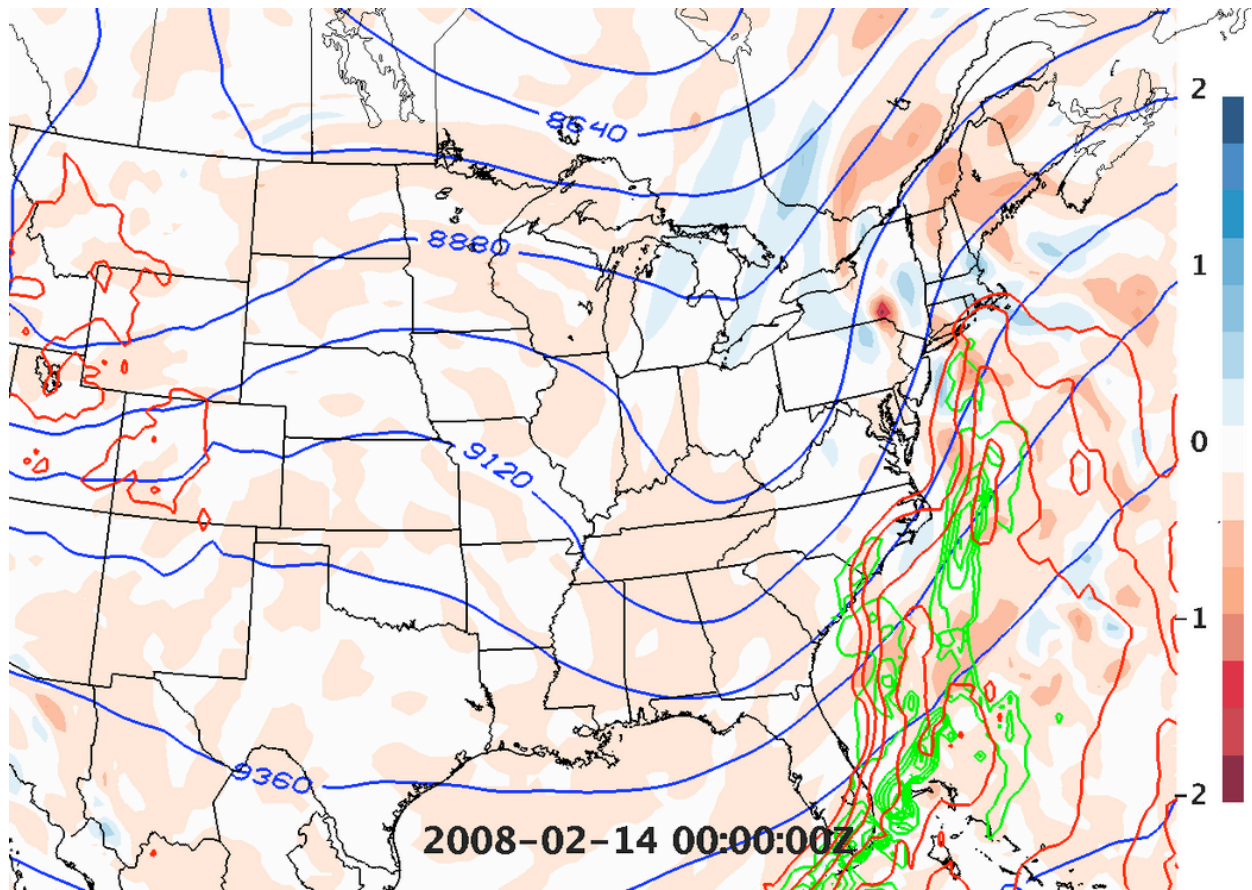


Figure 15. As in Fig. 8, but for 0000 UTC 12 February 2008 through 0000 UTC 14 February 2008, animated in 3-h increments.

NOTE: This figure is an animation. A representative image is shown above. [Link to animation.](#)

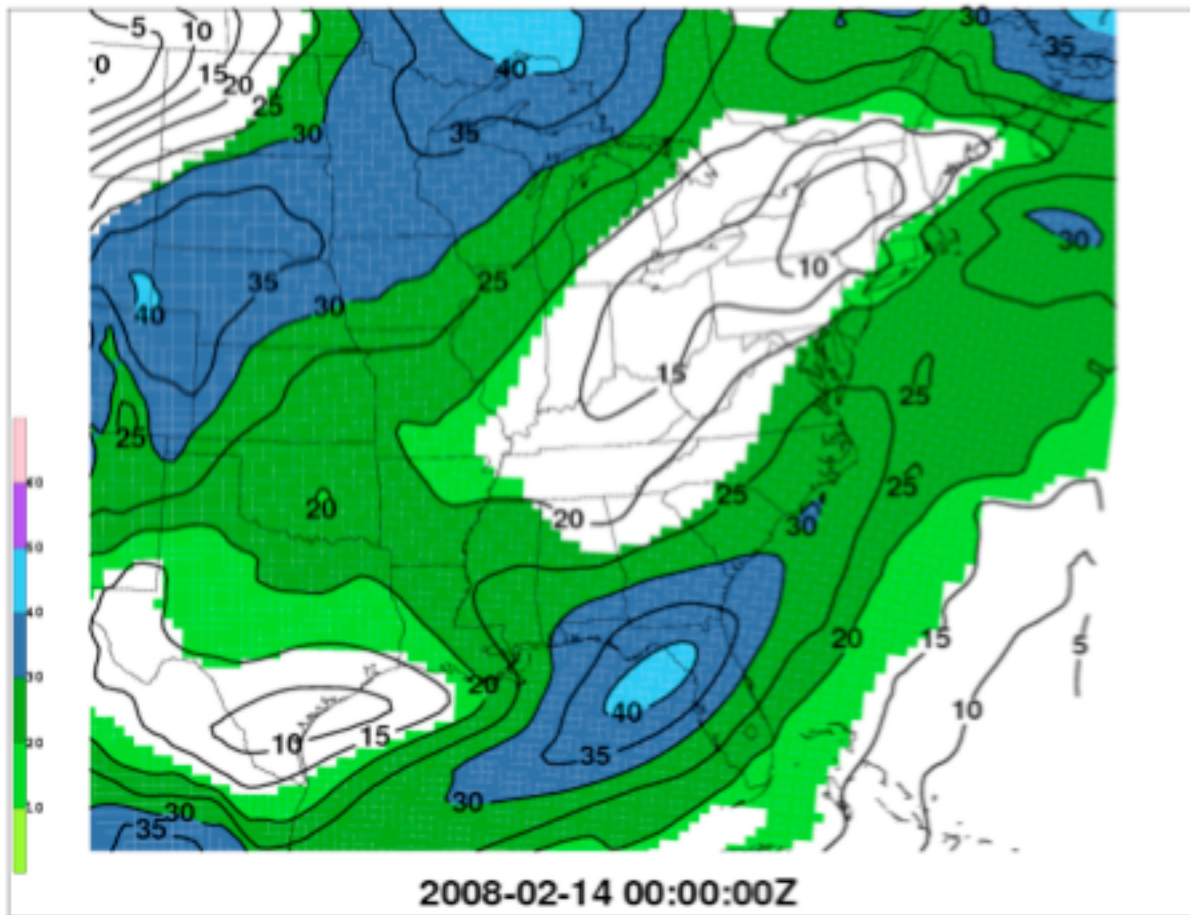


Figure 16. As in Fig. 9, but for 0000 UTC 12 February 2008 through 0000 UTC 14 February 2008, animated in 3-h increments.

NOTE: This figure is an animation. A representative image is shown above. [Link to animation.](#)

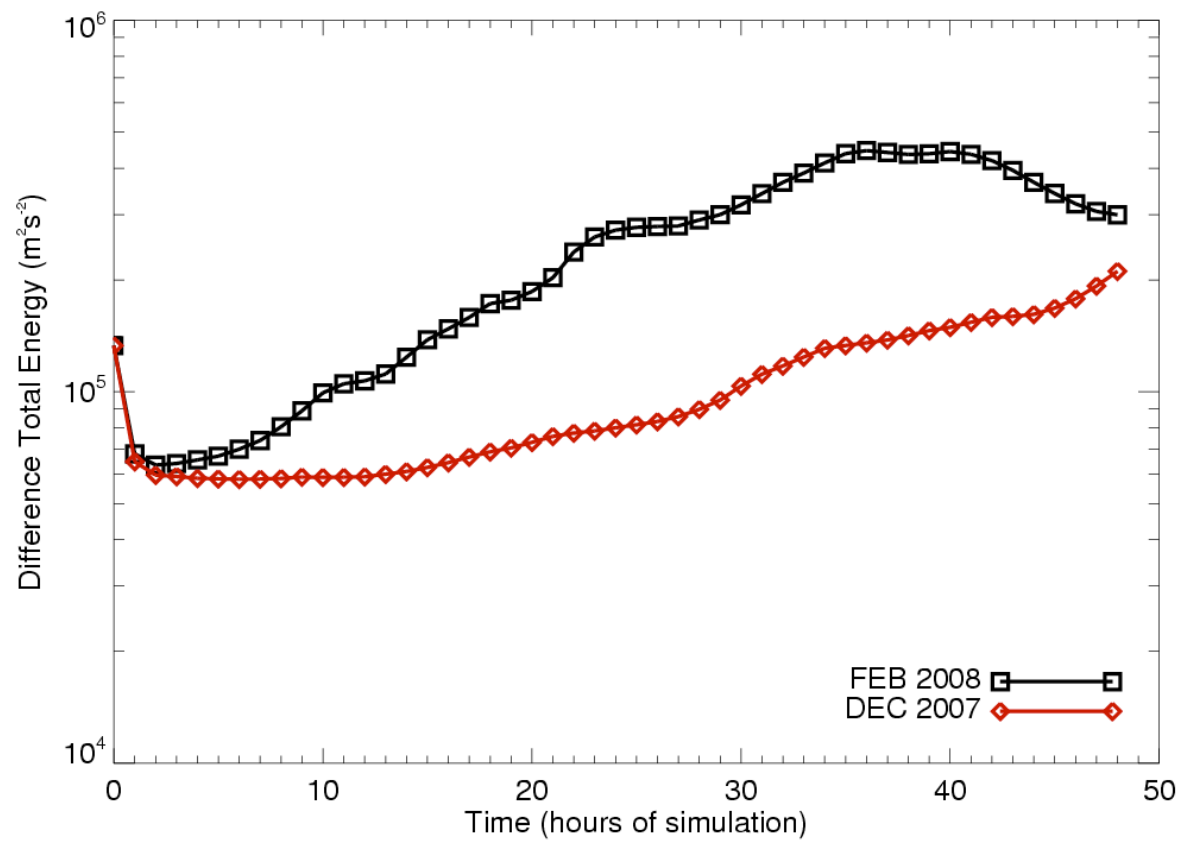


Figure 17. Evolution of Difference Total Energy (DTE) (m^2s^{-2}) over the 48-h forecast period (data presented hourly) for both cases, as indicated in the chart legend.

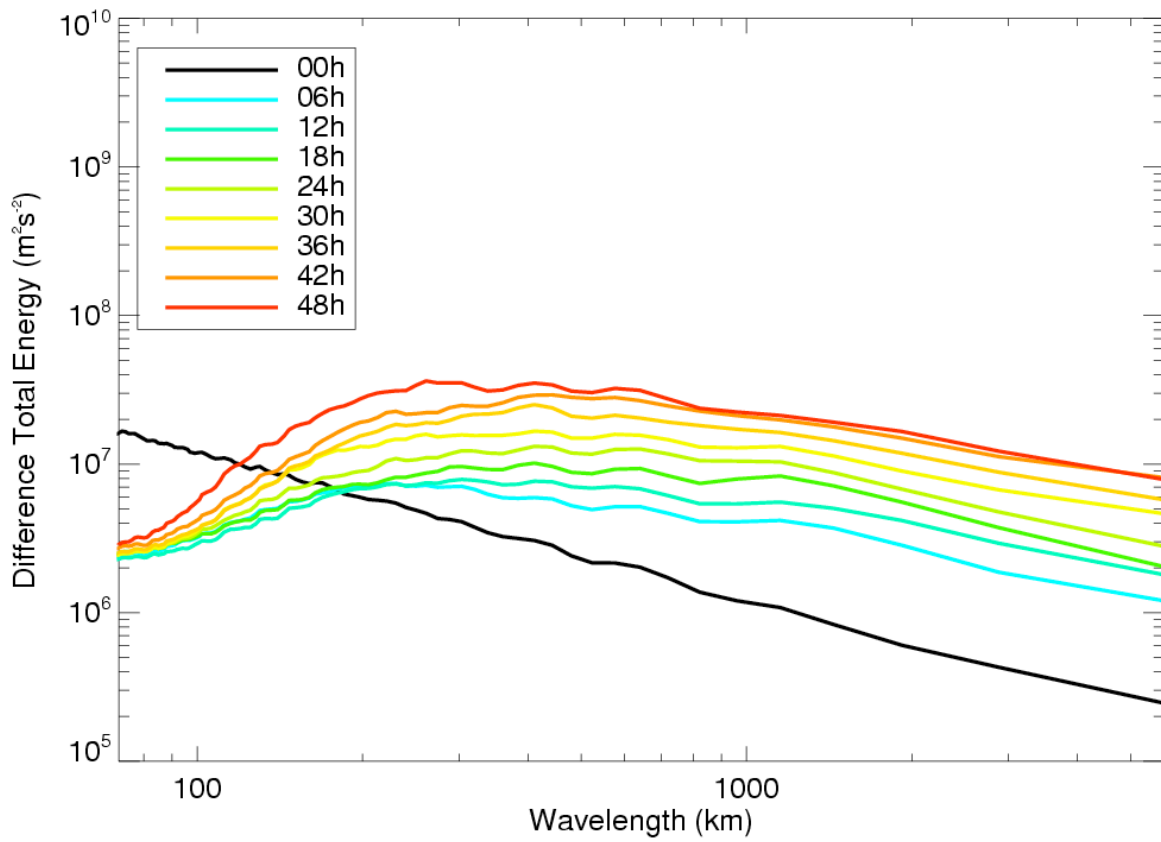


Figure 18. Power spectra of DTE (m^2s^{-2}) from December case plotted every 6 h, as indicated on chart legend. Vertical bar indicates peak wavelength for each time.

NOTE: This figure is an animation. A representative image is shown above. [Link to animation.](#)

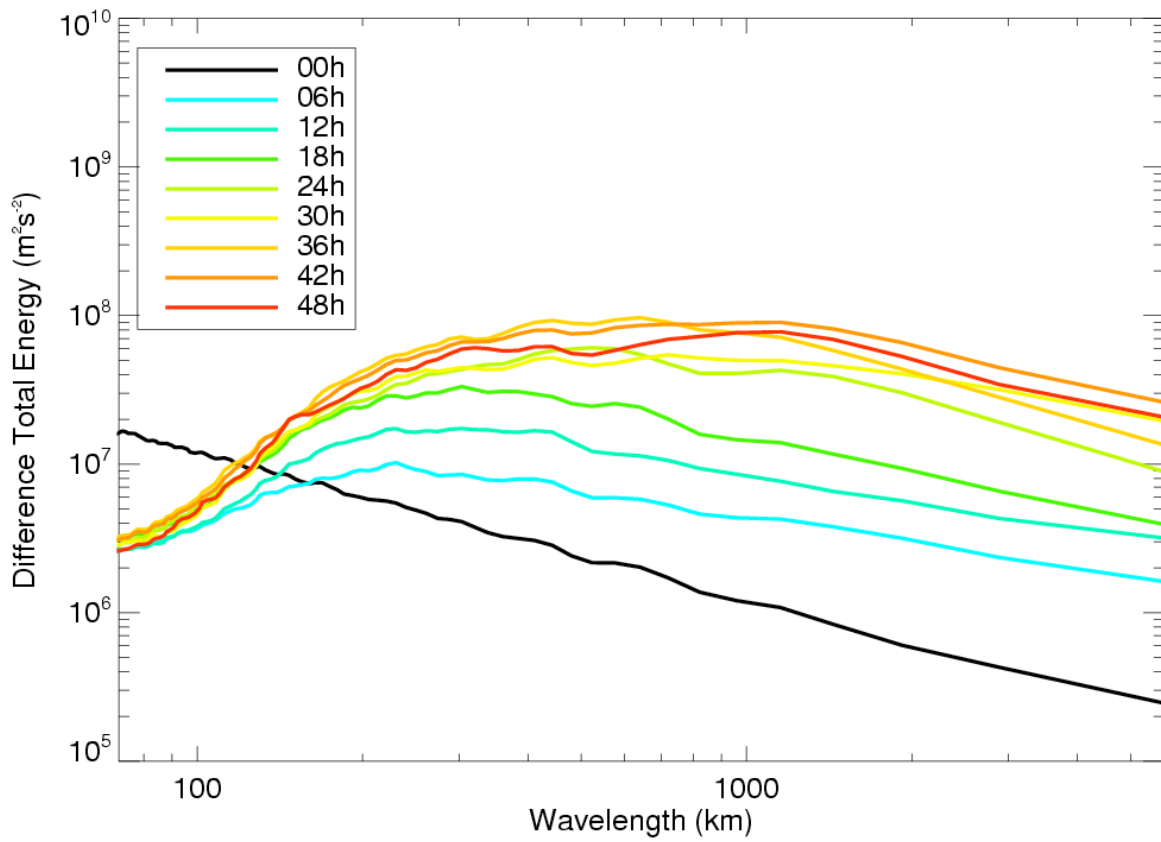


Figure 19. Power spectra of DTE (m^2s^{-2}) from February case plotted every 6 h, as indicated on chart legend. Vertical bar indicates peak wavelength for each time.

NOTE: This figure is an animation. A representative image is shown above. [Link to animation.](#)

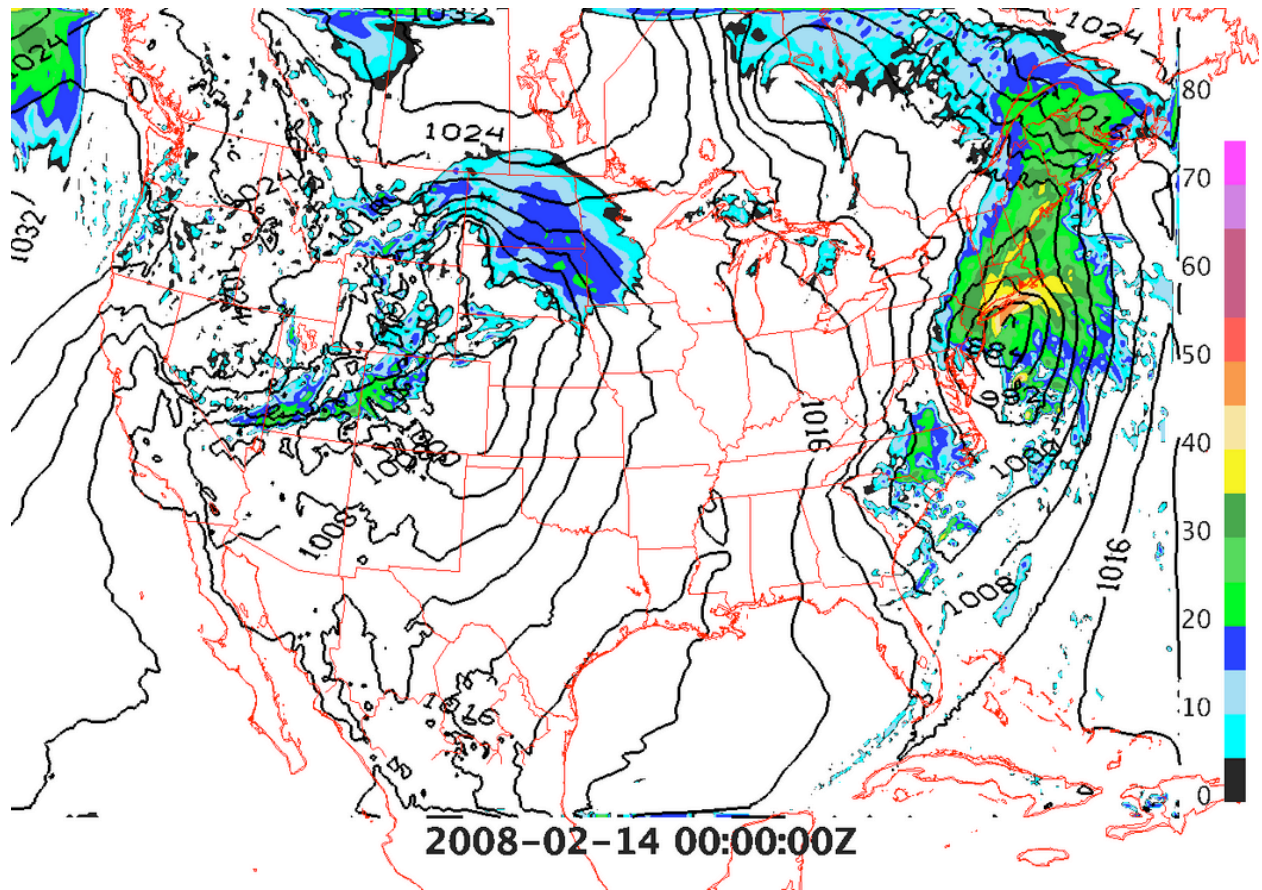


Figure 20. As in Fig. 11, but for 12-km forecast.

NOTE: This figure is an animation. A representative image is shown above. [Link to animation.](#)

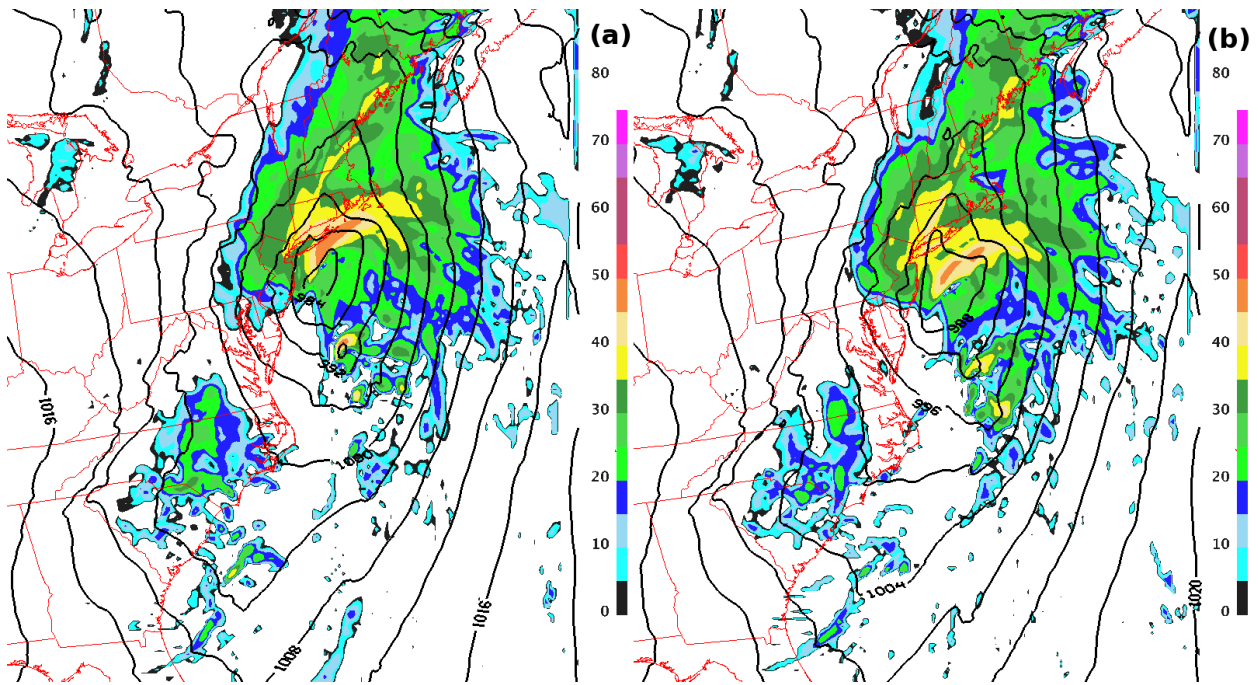


Figure 21. As in Fig. 12, but for 12-km forecast.

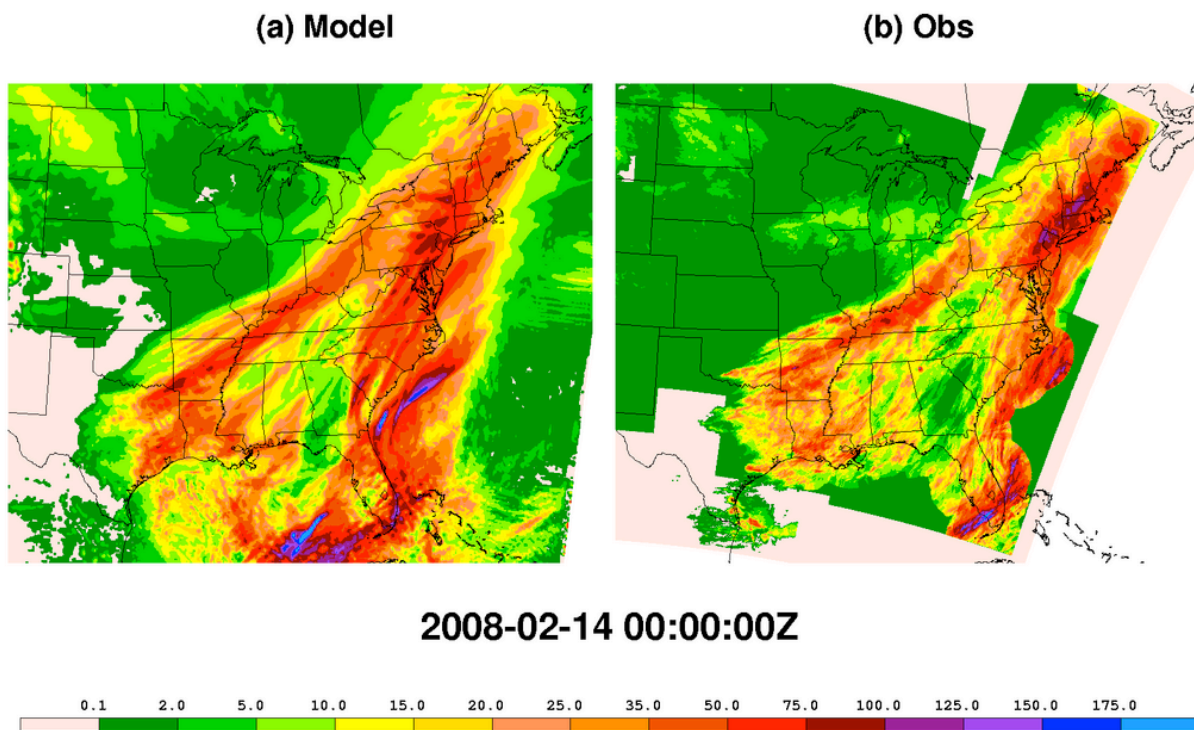


Figure 22. As in Fig. 13, but for 12-km forecast.

NOTE: This figure is an animation. A representative image is shown above. [Link to animation.](#)

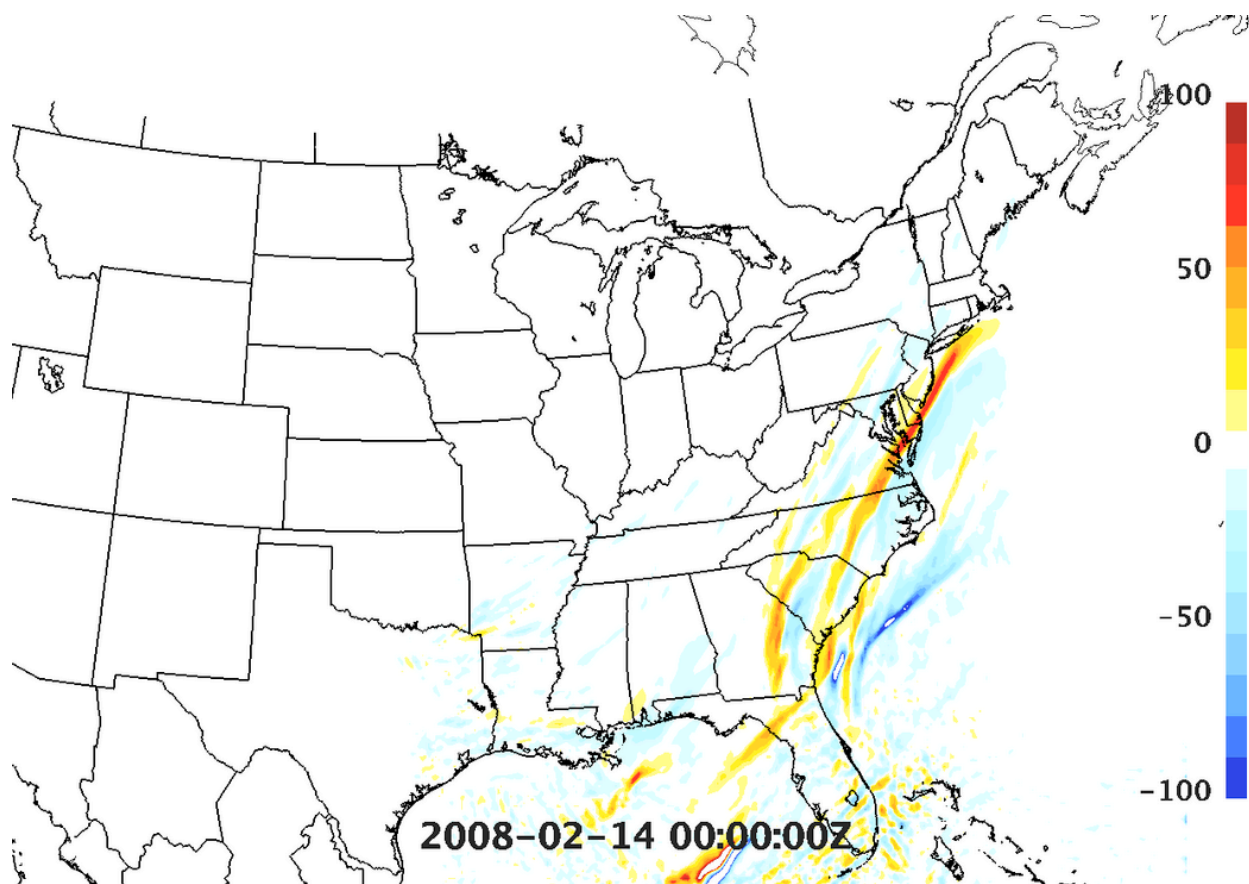


Figure 23. As in Fig. 14, but for 12-km forecast.

NOTE: This figure is an animation. A representative image is shown above. [Link to animation.](#)

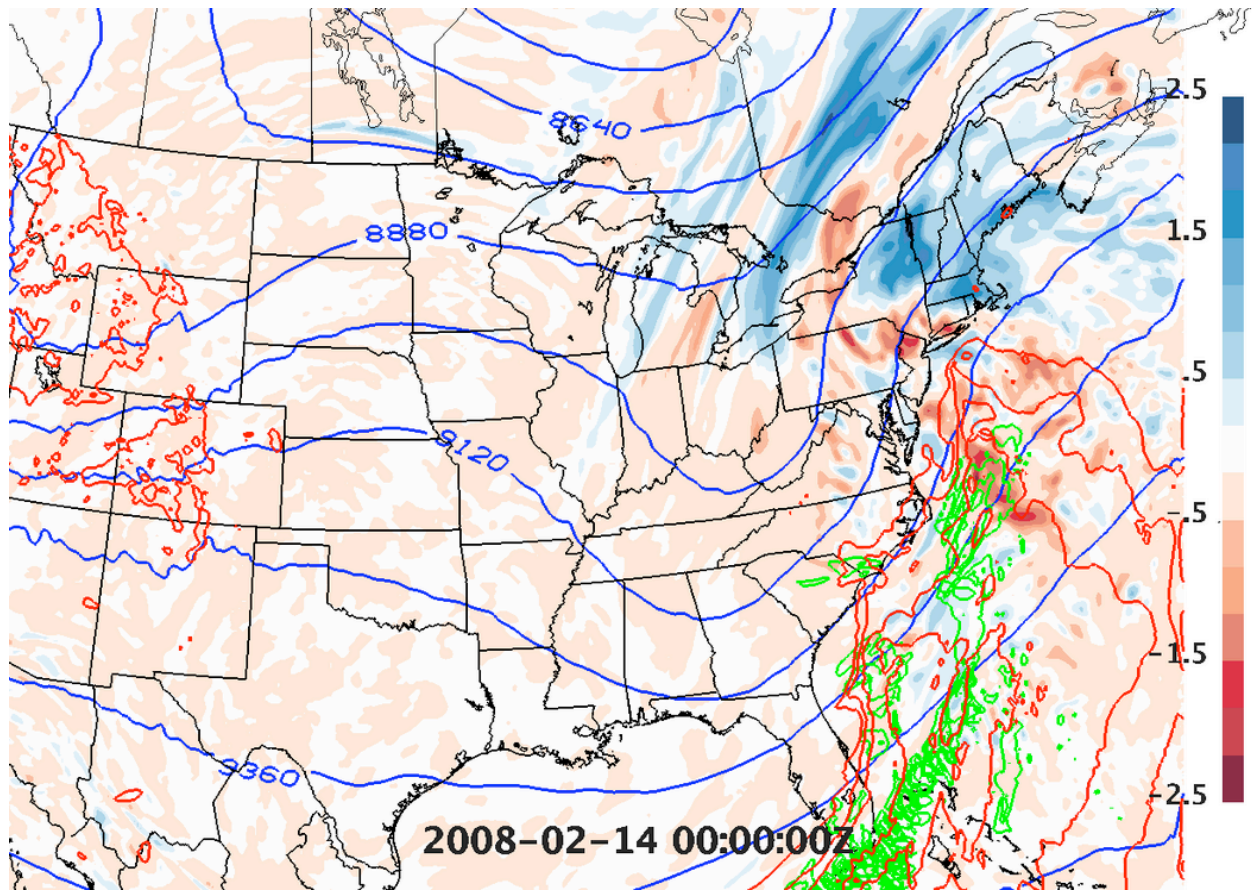


Figure 24. As in Fig. 15, but for 12-km forecast.

NOTE: This figure is an animation. A representative image is shown above. [Link to animation.](#)

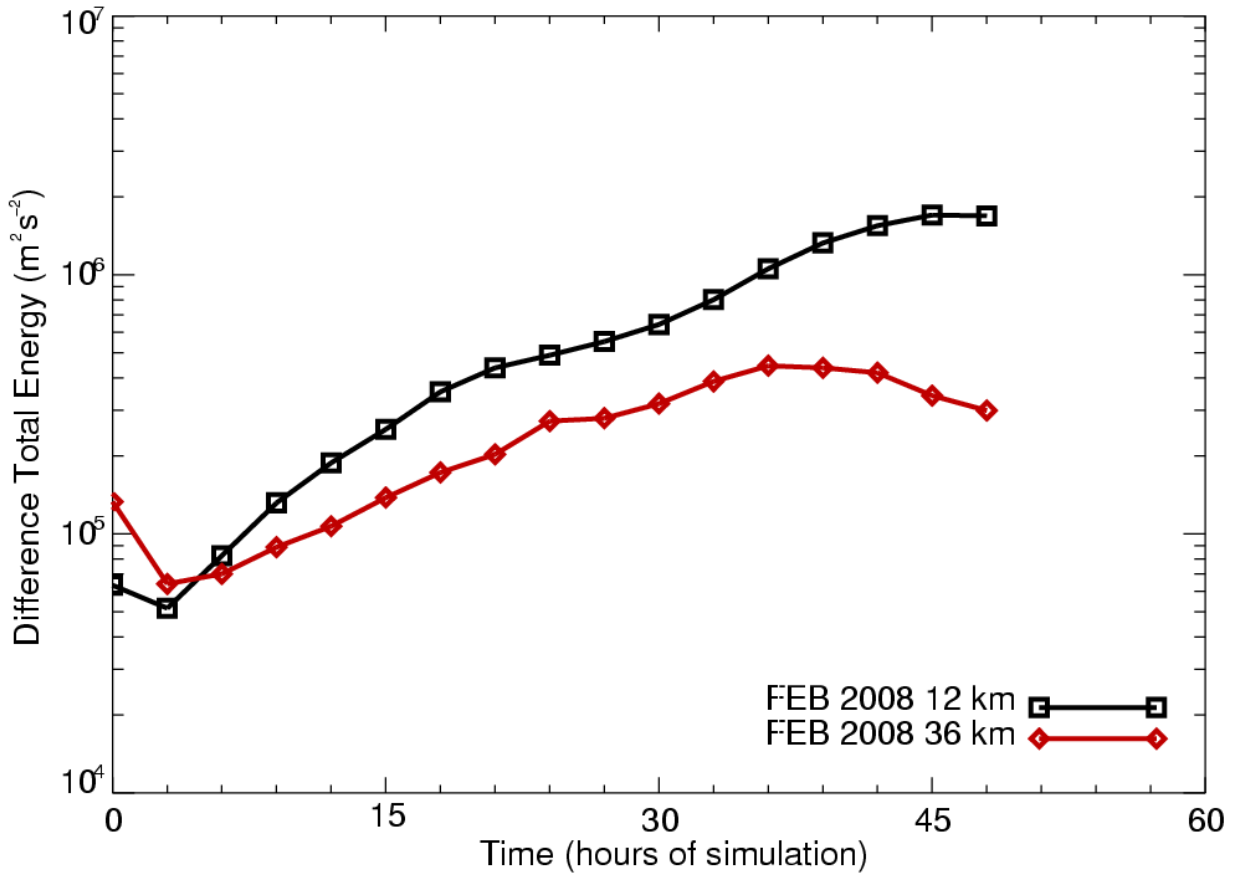


Figure 25. Evolution of DTE (m^2s^{-2}) over the 48-h forecast period (data presented every 3 h) for the 36-km and 12-km forecasts of the February case, as indicated in the chart legend. 12-km data have been interpolated to the 36-km grid for a more equivalent comparison.

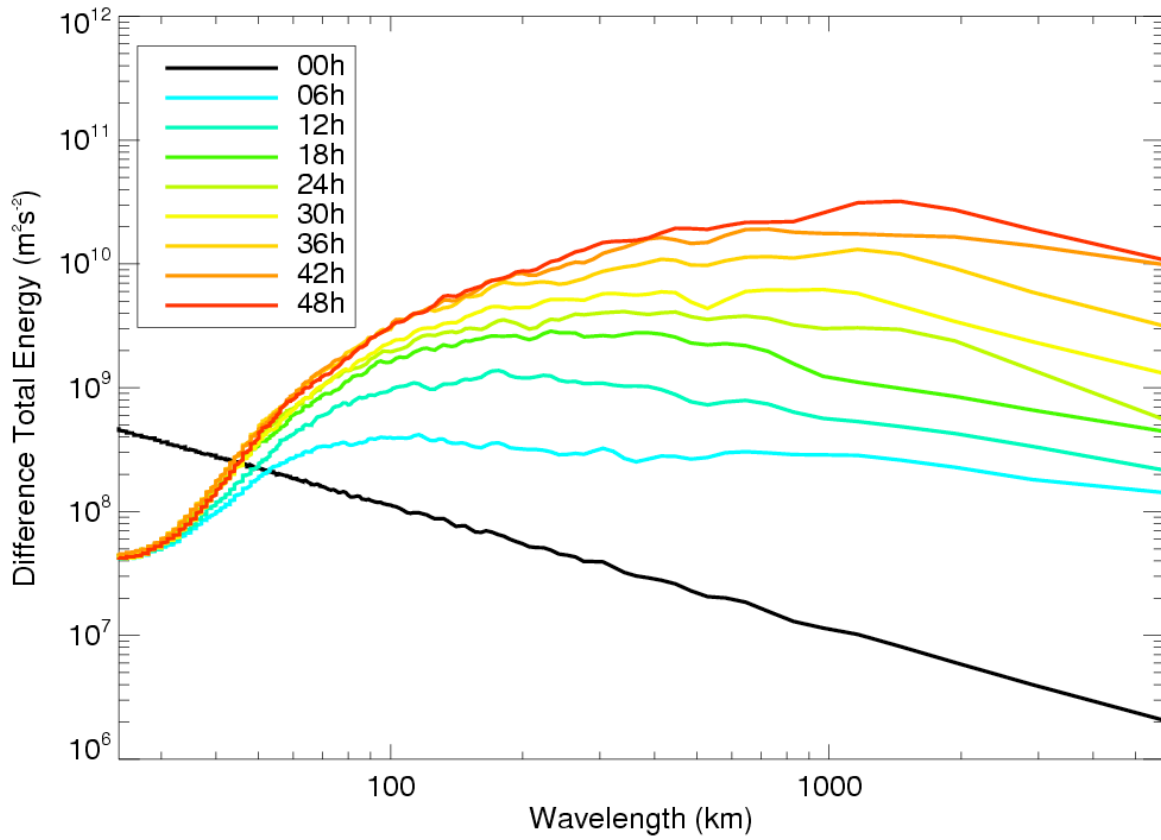


Figure 26. Power spectra of DTE (m^2s^{-2}) from February case run at 12 km and plotted every 6 h, as indicated on chart legend. Vertical bar indicates peak wavelength for each time.

NOTE: This figure is an animation. A representative image is shown above. [Link to animation.](#)